CHAPTER-5

RESULTS AND DISCUSSION

This research aims to analyze the characteristics of cavitation and its impact on spray formation. To attain the stated goal, a numerical and experimental investigation was conducted. The numerical work started with the validation of the existing numerical model against the benchmark experimental work of Winklhofer et al. [14]. Numerical modelling was extended to develop the two-step coupling method and implemented in the ECN spray C fuel hole injector. This novel approach considers the impact of inner nozzle cavitation on spray breakup. Due to restricted resources, it is not possible to get internal access to view cavitation in a real-size nozzle. To address this issue, a larger-scale nozzle was designed and cavitation flow was examined. The cavitation phenomena are characterized using water, diesel, and WCO-biodiesel. The operating and geometrical factors have been examined for cavitation-induced spray breakup. Finally, experimental and numerical work is performed to determine macroscopic spray characteristics. The findings were compared for diesel, WCO-biodiesel, and tallow-biodiesel.

5.1 RESULTS OF WINKLHOFER NOZZLE

5.1.1 Effect of Pressure difference

The current investigation is similar to the experiment conducted by Winklhofer et al. [14], in which the pressure differential was established identically. Injection pressure is kept constant at 100 bar in every case, whereas backpressure ranges from 15 to 80 bar, resulting in a pressure difference of 20 to 85 bar as shown in Fig. 5.1.

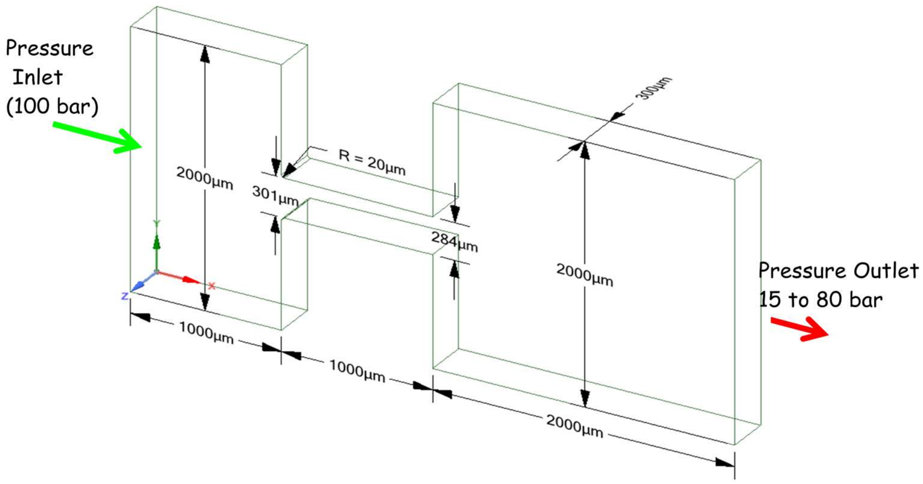

Fig. 5.1 Winklhofer nozzle with its boundary conditions

Large recirculation is forming near the nozzle entrance due to sudden contraction in the area. This recirculation zone generates a shear layer and a low-pressure region, which eventually leads to vapor bubble production near the throttle opening. Fig. 5.2 depicts the velocity curve in the transverse direction at 0.053 mm from the throttle entrance. The maximum velocity occurs in the shear layer, roughly 0.045mm away from the top and bottom walls; it then drops to a minimum value in the centre. The shear layer expanded as pressure differences increased. Fig. 5.3 depicts the pressure distribution along the central line.

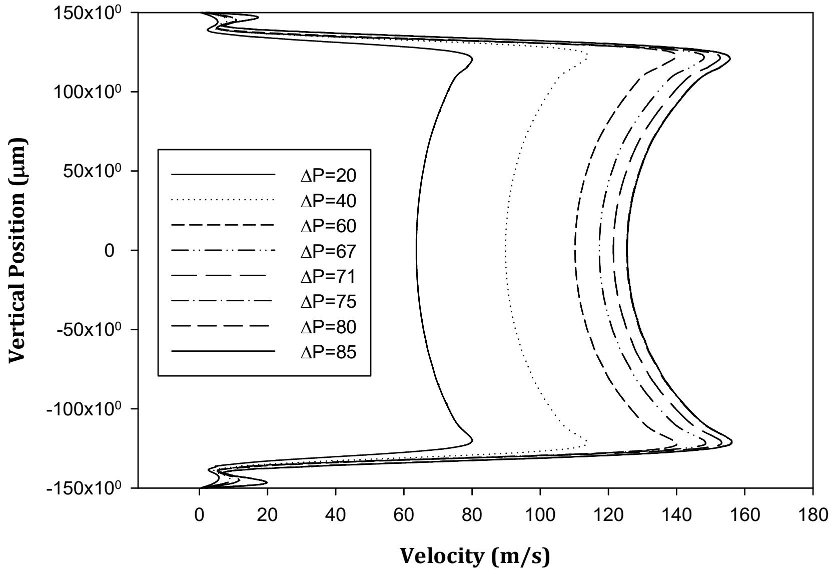

Fig. 5.2 Velocity profile at a location x=0.053mm from the nozzle inlet

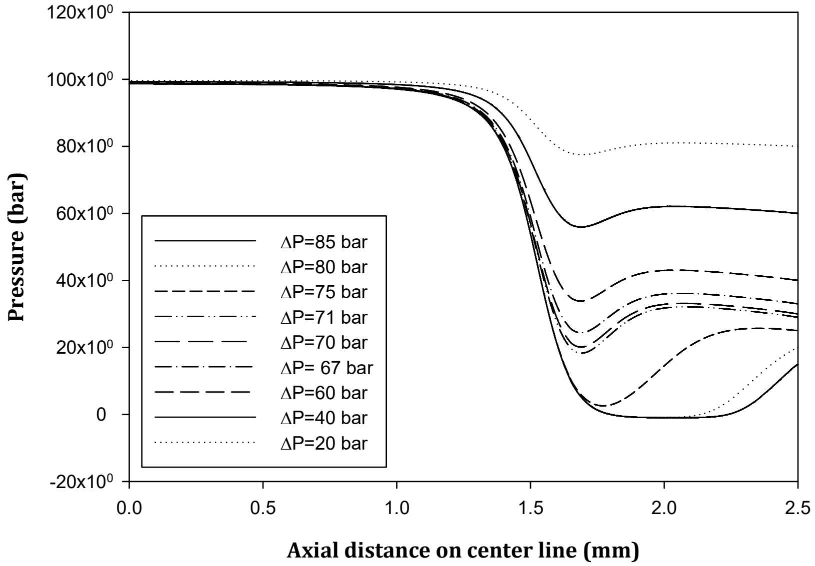

Fig. 5.3 Pressure distribution along with the axial distance

The pressure distribution along the nozzle wall is less than the pressure at the centreline. When local pressure falls below vapour pressure, bubbles start to form and move along the continuous flow. However, it collapses as pressure recovers and reaches levels greater than the vapour pressure. As the pressure differential increases, the low-pressure recirculation zone extends towards the throttle outlet.

The efficiency of the throttle can be decided based on the discharge coefficient. The fuel mass flow rate and the discharge coefficient have been calculated from simulation results at variable pressure differences.

$$C_d = \frac{\dot{m}_{actual}}{A\sqrt{2\rho(\Delta P)}} \tag{5.1}$$

Nurik [9] experimented with his transparent nozzle with varying upstream and downstream pressure and L/D ratios. Based on this work, he has proposed a one-dimensional theoretical model to predict discharge co-efficient given below:

$$C_d = C_c\sqrt{K} \tag{5.2}$$

$$K = \frac{P_{inj} - P_v}{P_{inj} - P_{back}} \tag{5.3}$$

Where K is the Cavitation parameter and C_c is the contraction coefficient. The values of C_c depend on geometrical parameters; for the sharp edge nozzle, it is 0.61, and for the rounded corner, it is between 0.61 to 1. The value of C_c can be calculated with the help of the equation proposed by Weishback [20].

$$C_c = 0.63 + 0.37\left(\frac{A_2}{A_1}\right)^3 \tag{5.4}$$

It is observed that the discharge coefficient decreases after cavitation inception and reaches its minimum value at super cavitation as shown in Fig. 5.4. Since the throttle has been choked after super cavitation, no further mass flow rate increases with pressure differences. It is interesting to note that the present data falls above the theoretical curves. This suggests the effect of rounding at the inlet increases the discharge co-efficient. Nurik's[9] theoretical model is based on the experimental work carried out with a sharp edge nozzle, which exhibits early cavitation inception (K=2). In Nurik's experiment, he observed hydraulic flip instead of super cavitation, which was the reason for the lower values of discharge co-efficient. A higher value of the cavitation parameter indicates the smaller differences between the injection pressure and backpressure, which is non-cavitation flow. During non-cavitating flow, the discharge coefficient is no longer a function of the cavitation parameter but depends on the Reynolds number. At a higher cavitation parameter value, the discharge coefficient stays fairly constant.

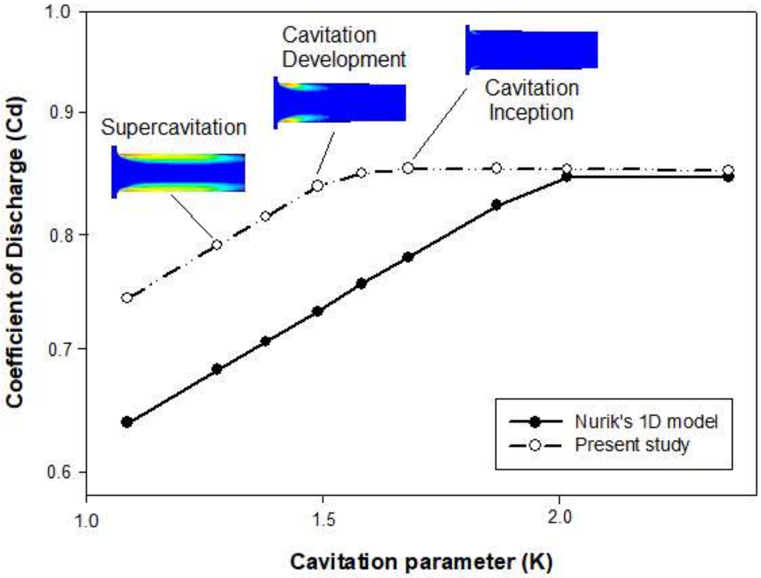

Fig. 5.4 Comparison of Discharge coefficient vs. Cavitation parameter with Nurik's theoretical model [9]

5.1.2 Effect of nozzle geometry

The conicity factor or *k-factor* has been used to evaluate the effects of nozzle geometry. Here *k-factor* measures the amount of taper and is defined as:

$$k - factor = \frac{D_{in} - D_{out}}{D_{in}} \times 100 \tag{5.5}$$

Where D_{in} and D_{out} are inlets and exit diameters of a nozzle in a micrometre, respectively, the positive *k-factor* represents the convergent nozzle, and the negative *k-factor* represents the divergent nozzle. The dimensions chosen are one of the experimental studies of Winklhofer et al. [14]; all geometries were kept with a constant inlet diameter of 301 µm. The nozzle with zero *k-factor* has the same inlet and exit diameters. In positive *k-factor*, exit diameter is 284 µm making *k-factor* = +5.65. Similarly, the negative *k-factor* exit diameter was kept at 318 µm with *k-factor* = -5.65. Generally, nozzles of positive and zero *k-factor* are used in the fuel injector. Since the negative *k-factor* nozzle is divergent and tends to reduce exit velocity, which may lead to poor atomization.

The effects of nozzle convergence on the mass flow rate are shown in Fig. 5.5. It is observed that the mass flow rate of the divergent nozzle is more than the convergent nozzle before cavitation inception. But this condition reverses after getting choked flow. As soon as the choking condition approaches, the area available to liquid is less in the divergent nozzle due to the thick cavitation layer, as shown in Fig. 5.6. But this is not the case in the convergent-shaped nozzle. The inertia of liquid wipes out the developed cavitation layer and maintains a thin layer. Hence, the available area in the case of the convergent nozzle at the choking condition is more than the divergent nozzle.

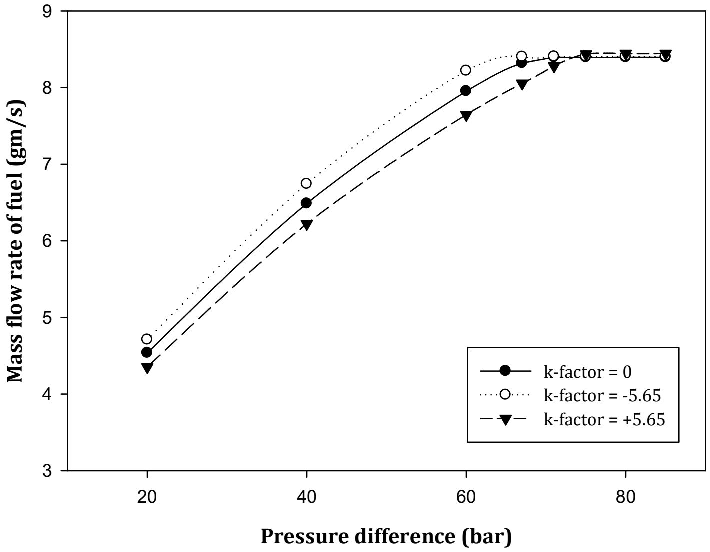

Fig. 5.5 Effect of *k-factor* on the mass flow rate of fuel at a variable pressure difference

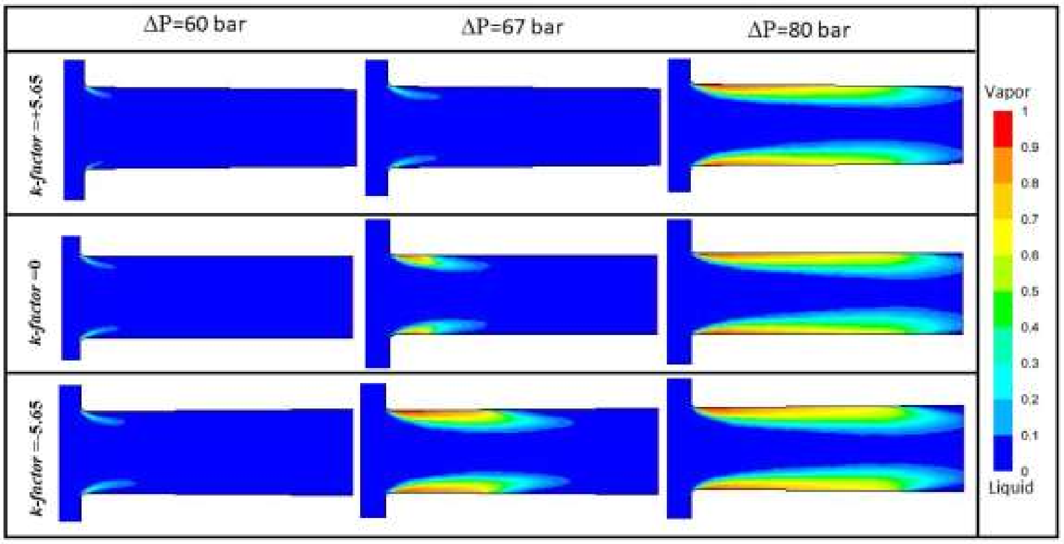

Fig. 5.6 Comparison of the vapor fraction contour at different *k-factor* values

5.3 Effect of fuel properties

The scarcity of petroleum and continuously increasing emissions encourage the use of bio-products. Bio-fuels are renewable, and that is the major advantage of it. Bio-diesel is a greener alternative to diesel. Due to its properties, its usage is limited. Here a study shows the effects of bio-diesel over cavitation phenomena. It is observed that the inception of cavitation in the case of diesel appears at a lower pressure difference (ΔP=60 bar) compared to bio-diesel (at ΔP=67 bar) as shown in Fig. 5.6. Due to higher liquid viscosity and lower saturation pressure, bio-diesel lags in cavitation inception. The amount of cavitation intensity is proportional to the effective area of the nozzle and thus the effective mass flow rate. The reduction in effective area increases with injection pressure. This finally reduces the nozzle's discharge coefficient. Because biodiesel has less cavitation, its overall mass flow rate and discharge coefficient are higher than those of diesel for the same pressure difference as illustrated in Fig. 5.7.

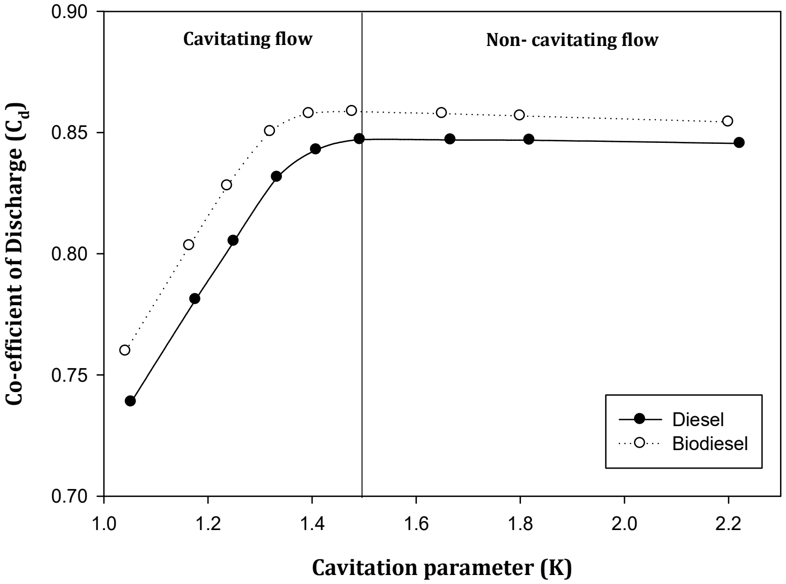

Fig. 5.7 Effect of cavitation parameter on discharge coefficient for diesel and bio-diesel

5.2 RESULTS OF ECN SPRAY C INJECTOR

Simulation of flow inside real-size modern injectors aids in understanding the injector's physical properties as well as the qualities of the emerging fuel. In this section, we look at single-hole injectors from the Engine Combustion Network injector series (210037C and 210003C) and simulate their performance. The engine combustion network (ECN) is an experimental and modelling collaboration aimed at improving computational fluid dynamic (CFD) modelling for engine-relevant situations at high temperatures and pressures. The five different series of Spray-C nozzles were manufactured to produce cavitation inside the nozzle intentionally. In the first section, the 210037C series was used to validate the results of the internal flow and prayer simulation. In the second portion, the 210003C series was used to simulate various operating conditions and the effects on internal flow and spray characteristics were assessed. The details of various simulation cases are listed in Fig. 5.8.

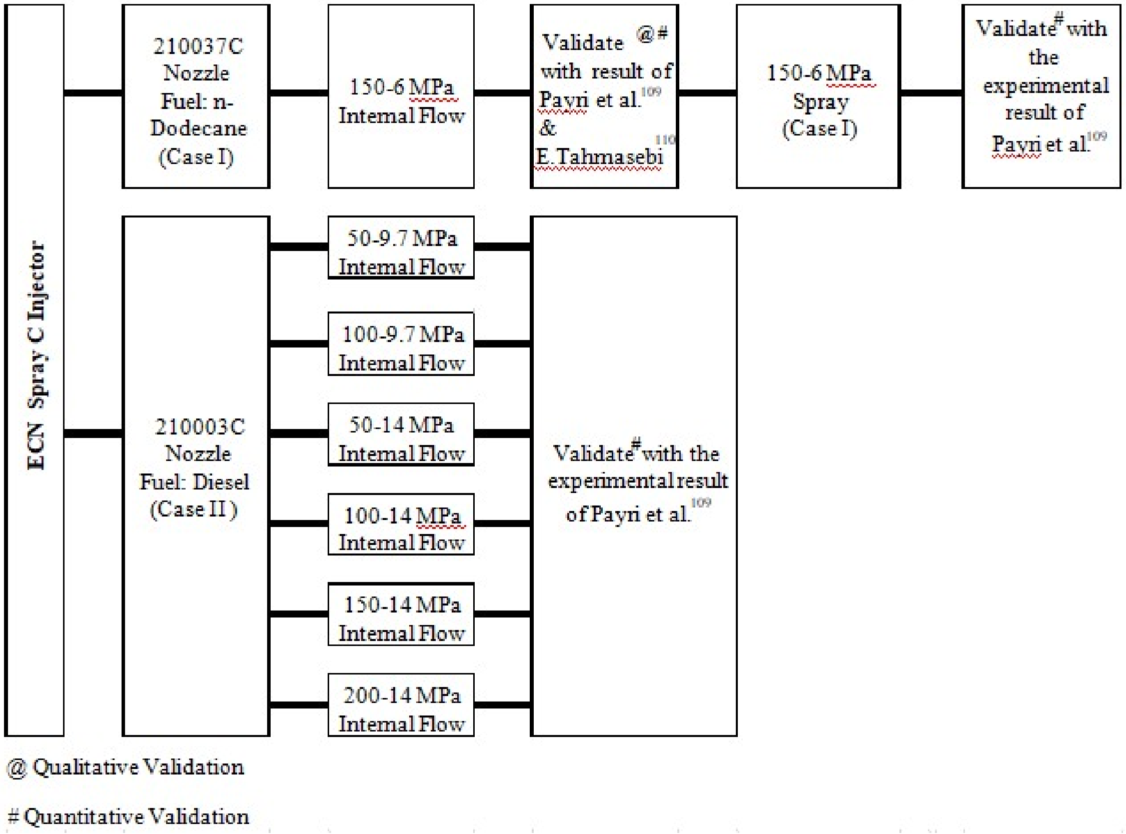

Fig 5.8 Details of various simulation case for Spray C injector

5.2.1 CASE-1 (ECN Spray 210037 C)

The geometry was used from the ECN network as discussed in chapter-4 and details of geometry is provided in section 4.3.1. Mesh sensitivity testing was undertaken, and adequate fine mesh was given at the nozzle entry. The injection pressure is assigned to be 150 MPa, with a nozzle exit pressure of 6 MPa. The internal flow simulation uses the VOF+ k-w SST+ZGB model combination. The simulation results were compared quantitatively and qualitatively to similar work by Payri et al. [54, 109] and Tahmasebi et al. [110]. Payri et al. [54, 109] experimented with a spray C injector and later developed the Eulerian-Eulerian single-step method for calculating the effect of cavitation on spray properties. Tahmasebi et al. [110] performed numerical simulations for the Spray C and Spray D injectors and compared the results of internal nozzle flow to the ECN database. This section's purpose is to fully validate the current work and demonstrate the consistency of the two-step coupled method.

The mass flow rate at the nozzle outlet was estimated and compared to similar work, which is reported in Table 5.1. Payri et al. [110] conducted trials with five distinct series of spray C nozzles to determine the rate of injection (ROI). The injection rate was determined using the injection rate discharge curve indicator (IRDCI). The recorded injection rate was amplified and converted from analogue to digital by the signal acquisition system. A total of 50 injection events were recorded, with an average mass flow rate of 10.10 grams/second. During each injection event, 45.2±0.2 milligrams of fuel are injected.

Table 5.1 Quantitative comparison of mass flow rate $\dot{m}$ (g/s)

Experimental Result Payri et al. [110]	Numerical Result of Payri et al. [54]	Numerical Result of Tahmasebi et al. [110]	Present study	
			Before area correction	After area correction
10.10 ± 0.1	11.42	10.51	11.54	10.00

In the current study, the mass flow rate is computed and compared to previous research. Simulation results predict a larger mass flow rate than experimental data. In the simulation, the mass flow rate is computed based on a fixed outlet area, however, during cavitation, the effective outlet size is reduced, potentially lowering the actual mass flow rate. To obtain accurate findings, add correction in the effective outlet area. The pixel method is used to obtain the effective diameter. The mass flow rate is calculated after area correction is shown in Fig. 5.9. After using correction factor the value of mass flow rate reach closer to the experimental results of Payri et al. [110]

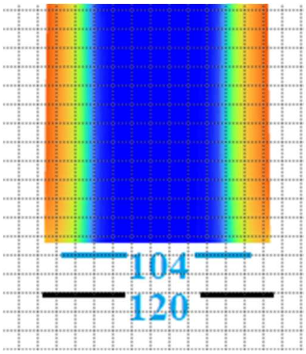

Outlet diameter = 120 pixel
Effective diameter for liquid = 104 pixel
Correction factor= 104/120 = 0.866
Effective mass flow rate = 0.866 * 11.54 = 10.00 g/s

Fig. 5.9 Pixel method to calculate effective diameter

Fig. 5.10 exhibits a qualitative comparison of various results with those of Tahmasebi et al. [110]. A comparison of pressure, velocity, vapor fraction contour, and pressure distribution along the axis has been shown. The upper portion of the results shows Tamasebi et al. [110] work, whereas the lower portions represent the results of the current investigation. All results show good consistency with the published work.

The detailed results for ECN spray-C are provided in Fig 5.11. Fig. 5.11 (a) depicts the variation in absolute pressure inside the injector flow passage with full needle lift. The n-dodecane fuel is injected at a pressure of 150 MPa. The pressure remains nearly constant until it enters the nozzle portion, revealing sac volume as a reservoir with almost constant pressure.

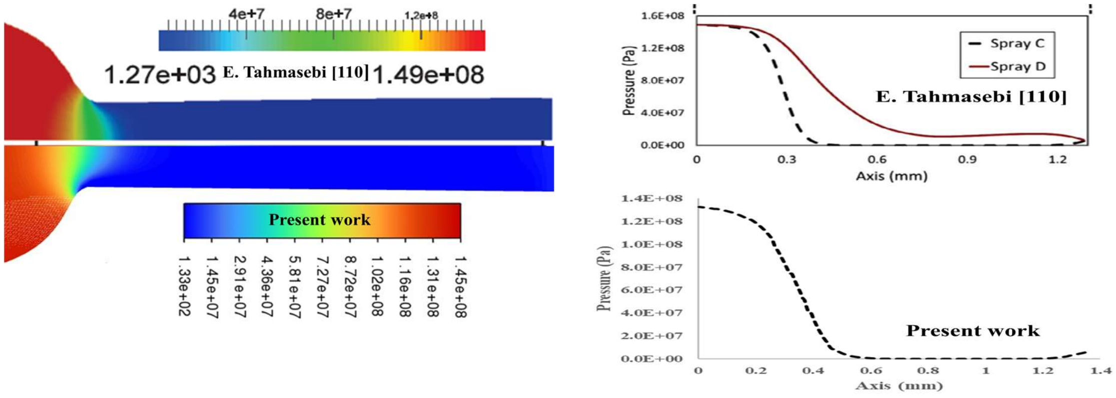

(a)Pressure contour (b) Pressure distribution along the axis

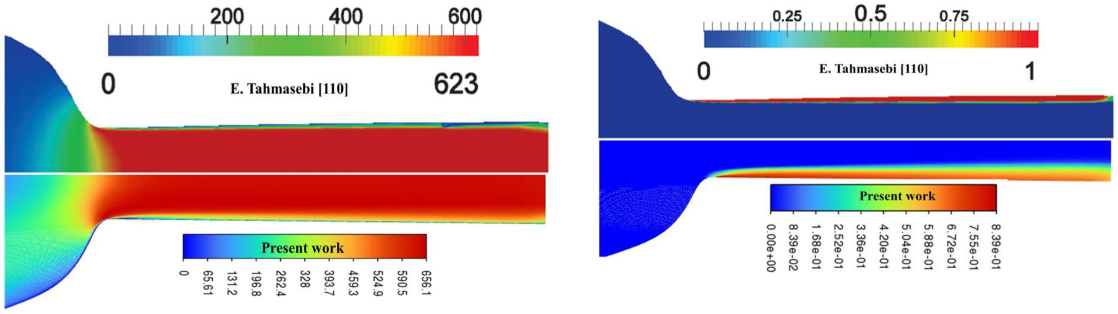

(c) Velocity contour (d) Volume fraction of vapour contour

Fig 5.10 Qualitative comparison of the simulation result with Tahmasebi et al. [110]

The velocity curve (Fig. 5.11(b)) confirms this, as the velocity is quite low near the sac volume. When fuel enters the injector nozzle, it accelerates due to an abrupt reduction in area, resulting in a drop in local pressure. The nozzle entry creates a huge recirculation and velocity fluctuations. Fig. 5.11(c) depicts the amount of turbulent kinetic energy. A high amount of turbulent kinetic energy is visible at the nozzle entry, owing to a large fluctuation in velocity. Finally, the local pressure drops below the fuel's vapor pressure and fuels begin to convert into vapor bubbles that move along the continuous flow; which is referred as cavitation. Fig. 5.11(d) shows the vapor fraction inside the nozzle. The red colour denotes the vapor phase, while the blue colour represents the liquid phase.

As discussed in the previous chapter, the parameters at the outlet of the nozzle have been calculated and an injection file has been created for spray simulation. These include coordinate position, velocity, diameter, temperature, and mass flow rates. These parameters are calculated in each grid cell of the outlet cross-section and then stored in a *.inj file. The total number of grid cells at the outlet is 150, and for each cell, a parameter has been obtained assuming a steady-state condition. This injection file has been used to define injection in the discrete phase model (DPM). The turbulent kinetic energy (ε) and turbulent dissipation rate (ω) are assigned at the inlet boundary condition using profile data.

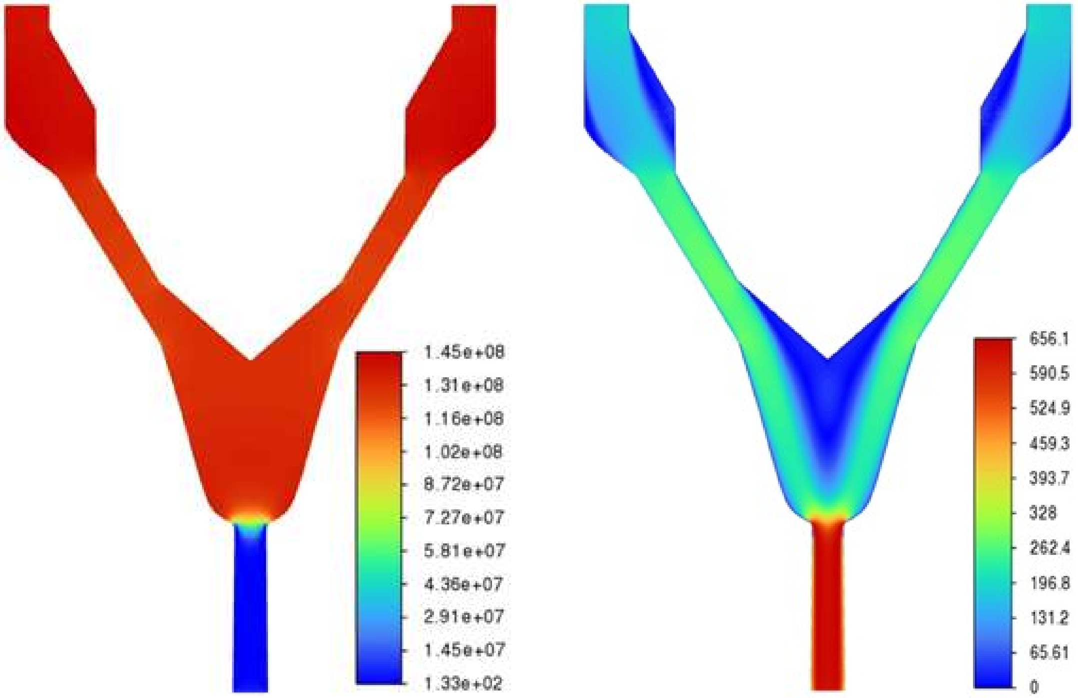

(a)Static Pressure contour in Pa (b)Velocity contour in m/s

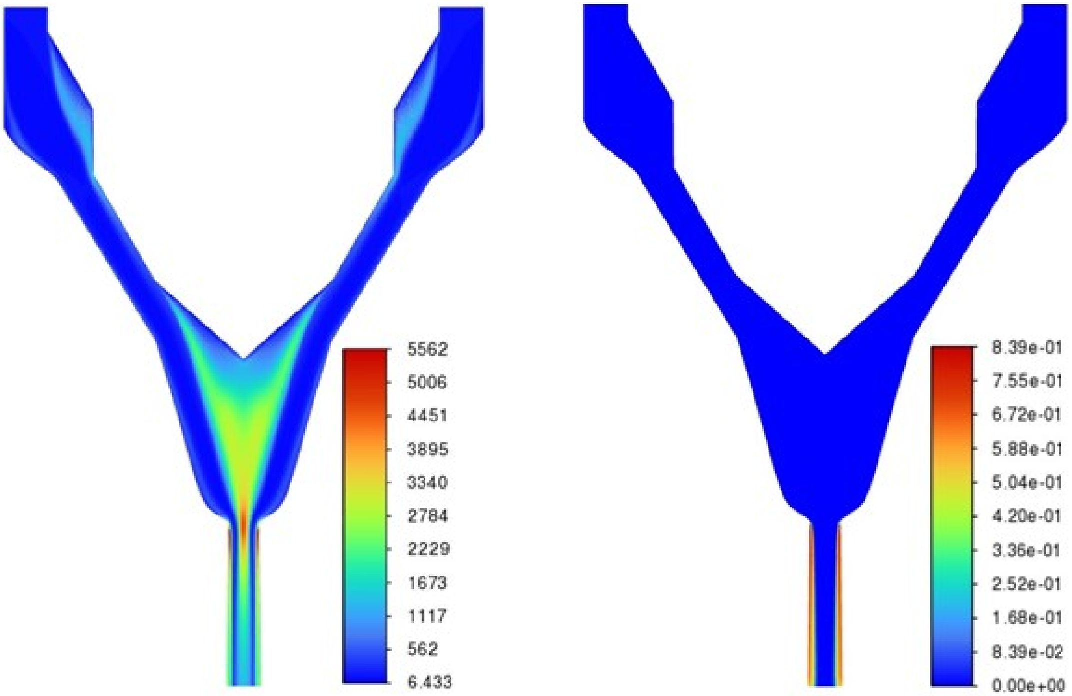

(c)Turbulent kinetic energy contour in m^2/s^2 (d)Volume fraction of vapour contour

Fig 5.11 Results contour for ECN spray C injector (Case-1)

For spray simulation, a Lagrangian-based DPM model has been used. ANSYS-Fluent's discrete phase calculations depend on initial conditions defining particle stream positions, velocities, and physical effects, which may require additional particle properties. To specify the initial conditions for a particle/droplet stream, create an "injection" and assign properties to it. In present method injection is assigned in terms of "file injection" type. The file injections may work in two ways, depending on the file format: A steady file can be applied to both steady and unsteady particle tracking. In the former instance, each line entry in the file generates a new particle parcel for each injection time step, as normal. By default, injection time steps match global fluid-flow time steps. An unstable file is only suitable for unsteady particle tracking. Each line entry in the file includes a time step. In the current work, a steady file was employed to avoid handling enormous amounts of data and reduce computational time. The steady file for a file injection requires the following format:

```
((x y z u v w diameter temperature mass-flow) name)
```

All of the words represent numerical parameters in scientific floating-point notation in SI units. All parentheses are necessary, but the name is optional. Table 4.2 lists the chamber conditions for spray simulations. Fig. 5.12 depicts the near-nozzle flow behaviour in terms of DPM concentration and spray velocity. The results demonstrate that the jet core has a larger concentration of fuel and velocity, as well as radial diffusion of liquid fuel.

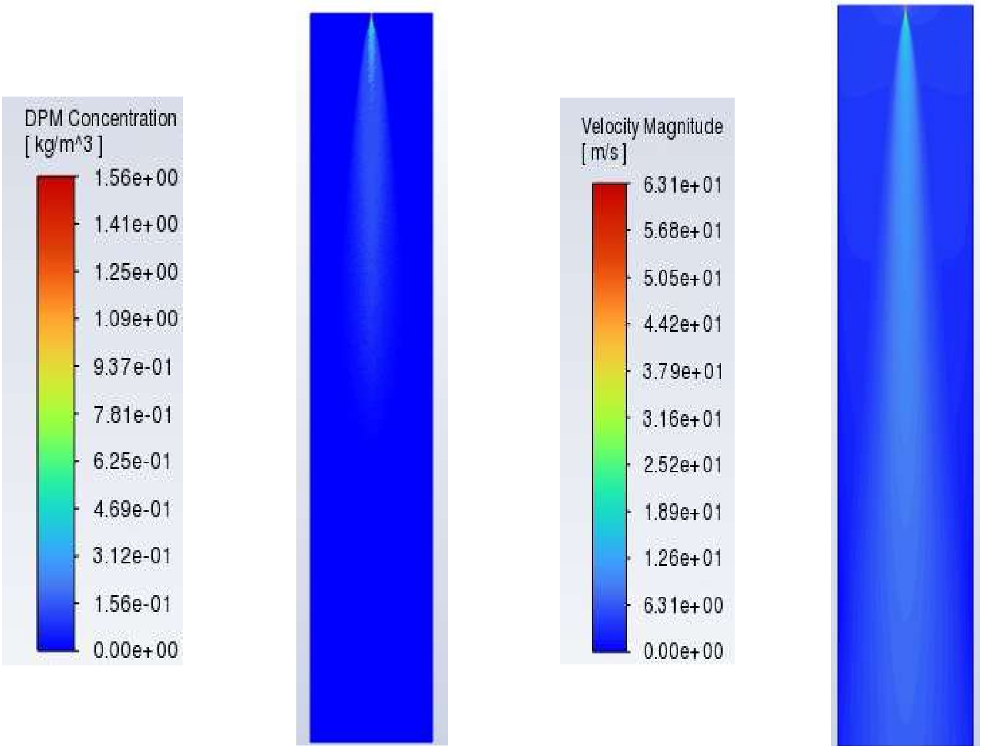

Fig 5.12 DPM concentration and velocity of spray

To validate the two-step coupled method, simulation results were compared to the experimental results of Payri et al. [109]. The injection file replicated the actual condition, and DPM performed better in predicting spray features, notably spray cone angle. Fig. 5.11 (d) shows that cavitation bubbles reach the nozzle output, indicating super cavitation. These vapour bubbles have a higher turbulent strength, which can affect spray cone angle. Fig. 5.13 depicts spray developments from spray simulation; the spray cone angle was measured after detecting the spray boundary. Table 5.2 shows the quantitative comparison of spray cone angle. The angle measured with present method is closer to the experimental results.

Table 5.2 Quantitative comparison of spray cone angle

Experimental Result of Payri et al.[110]	Numerical Result Of Payri et al. [54]	Present method
17.78°± 1.01°	18.76°	**17.09°**

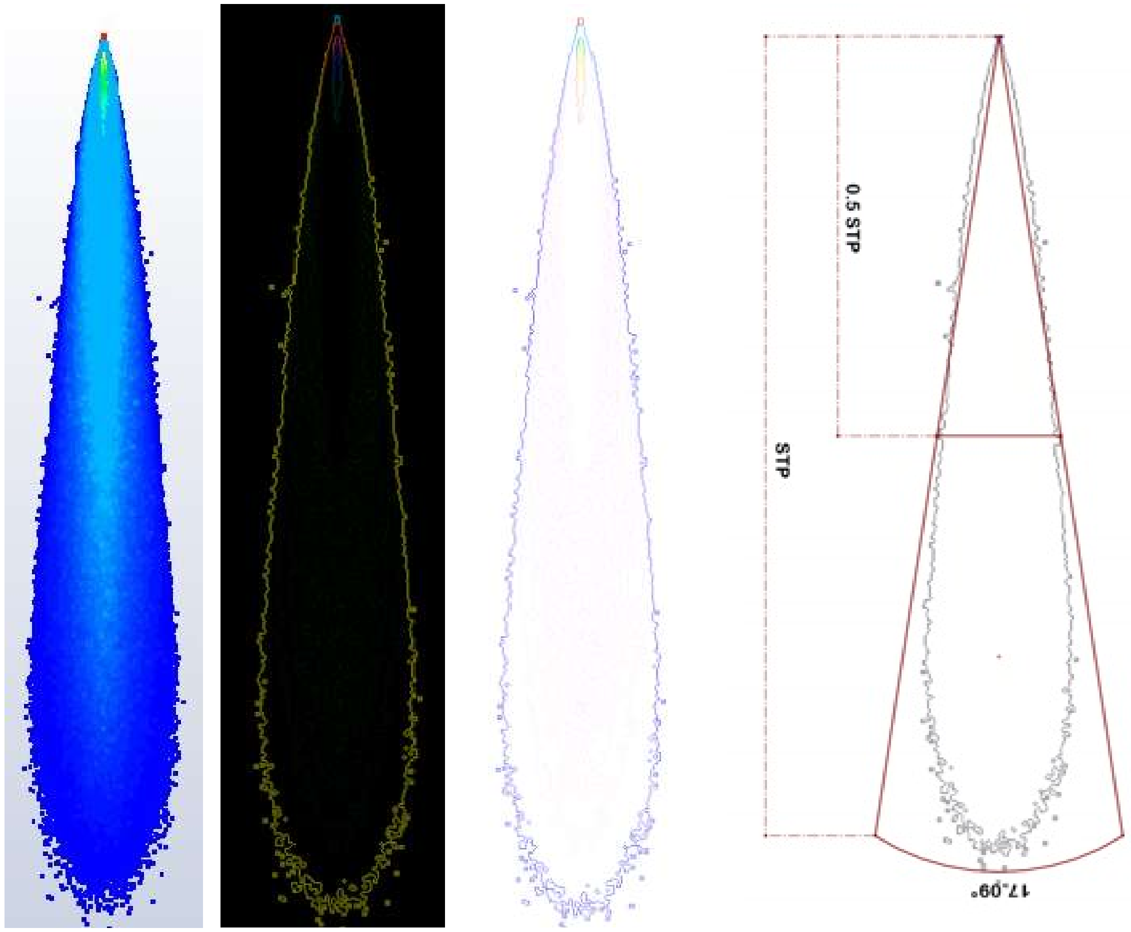

CFD image Edge detection Invert color Angle measurement

Fig 5.13 Steps for image processing and spray cone angle

5.2.2 CASE-2 (ECN Spray 210003 C)

The ECN spray C 210003 series injector was used to investigate the influence of inlet and outlet pressures. A simulation was performed with six distinct combinations of inlet and output pressure. The previous chapter examined the impact of the turbulence model on (1) k-ε RNG (Renormalization Group), (2) k-ε REALIZABLE and (3) k-ω SST (Shear Stress Transport). The results align better with the k-ω SST turbulence model. In this part, we compare the k-ω SST model to the k-ε Standard turbulence model and compare the results with Payri et al. [109] experimental study.

The k-ω (k-omega) SST (Shear Stress Transport) model is a hybrid turbulence model that incorporates the benefits of the k-ω and k-ε models. The k-ω SST model begins with the k-ω formulation in the near-wall region and gradually transitions to the k-ε formulation in the outer zone of the flow. The SST formulation contains a mechanism for accurately capturing the transportof turbulent shear stress. This is particularly helpful for predicting the turbulent eddies and flow structures caused by recirculation and cavitation. Fig. 5.14 presents the vapour fraction contour obtained using the k-ε (standard) and k-ω (SST) turbulence models. The results reveal that k-ε does not accurately forecast the degree of cavitation near the nozzle wall. As the pressure differential rises, the cavitation bubbles travel toward the nozzle outlet, a phenomenon known as super cavitation. The super cavitation occurs at ΔP=86 MPa with k-ω and ΔP=90.3MPa with k-ε turbulence models.

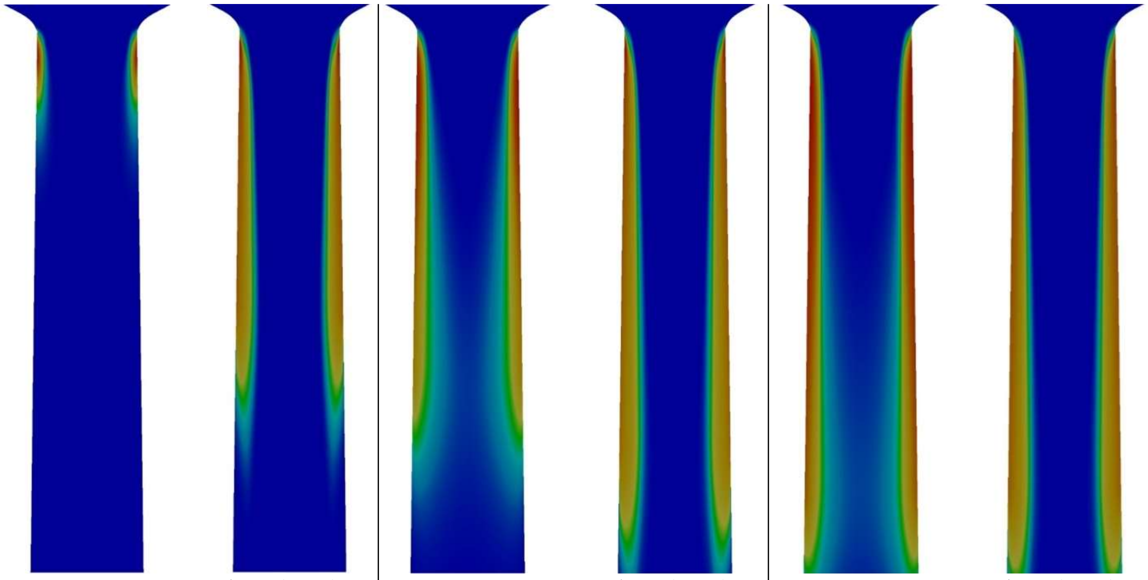

k-ε (Standard) k-ω (SST)

P_{inj}= 50MPaP_{back}= 14MPa

k-ε (Standard) k-ω (SST)

P_{inj}= 50MPaP_{back}= 9.7MPa

k-ε (Standard) k-ω (SST)

P_{inj}= 100MPaP_{back}= 14MPa

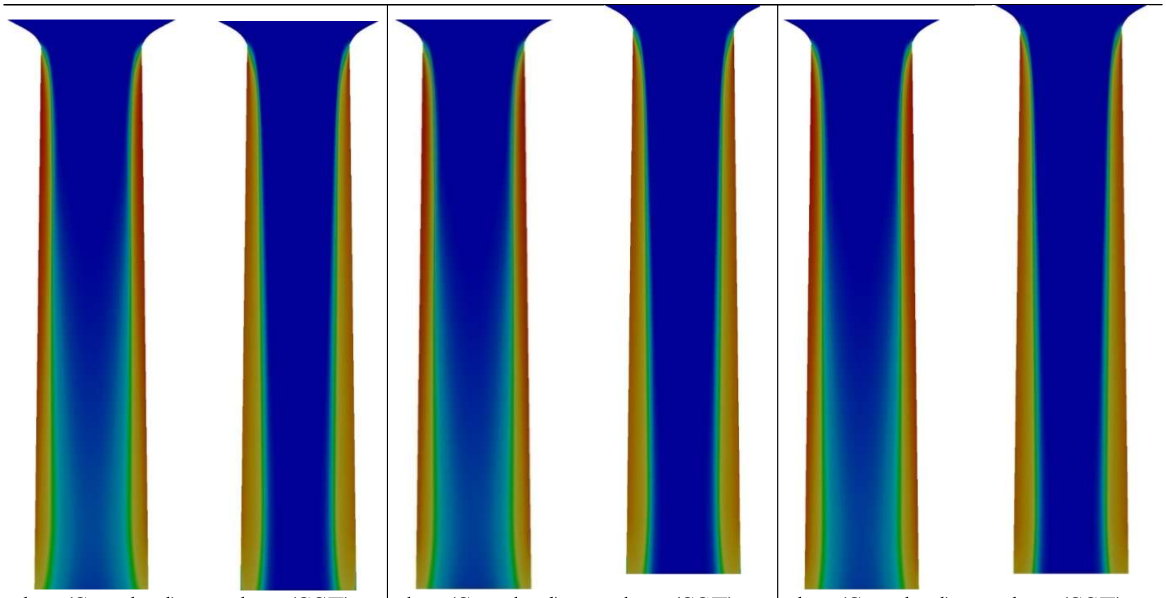

k-ε (Standard) k-ω (SST) P_{inj}= 100MPaP_{back}= 9.7MPa

k-ε (Standard) k-ω (SST) P_{inj}= 150MPaP_{back}= 14MPa

k-ε (Standard) k-ω (SST) P_{inj}= 200MPaP_{back}= 14MPa

Fig 5.14 Vapor fraction contour with different pressure and turbulent mode

Table 5.3 shows the calculated data for the exit velocity of fluid, mass flow rate, and effective diameter at different inlet and outlet pressures. The results are obtained using the k-ε and k-ω turbulence models and compared with the experimental data of Payri et al. [109].

Table 5.3 Quantitative comparison of present results with experimental data of Payri at el. [109]

P_{inj} MPa	P_{back} MPa	ΔP MPa	V (k-ε) (m/s)	V (k-ω) (m/s)	V (Exp.) (m/s)	$\dot{m}$ (k-ε) (kg/s)	$\dot{m}$ (k-ω) (kg/s)	$\dot{m}$ (Exp.) (kg/s)	D_{eff} (CFD) mm	D_{eff} (Exp.) mm
50	14	36	254	262	---	7.3433	7.2707	6.3010	212.0	---
50	9.7	40.3	260	280	260	7.3782	7.2706	---	203.1	---
100	14	86	402	415	---	10.4362	10.3388	8.874	191.8	---
100	9.7	90.3	416	429	408	10.4362	10.3388	---	182.6	180.0
150	14	136	516	528	532	12.8334	12.6937	10.8330	181.4	179.0
200	14	186	609	622	604	14.8481	14.6836	12.6010	176.3	177.5

However, quantitative calculations yield similar results for both turbulence models depicted in Fig. 5.15 and Fig. 5.16. The computed exit velocity and mass flow rate are quite similar with both turbulence models. The k-ε and k-ω turbulence models estimate exit velocity that closely matches experimental data. It demonstrates that CFD accurately predicts velocity magnitude.

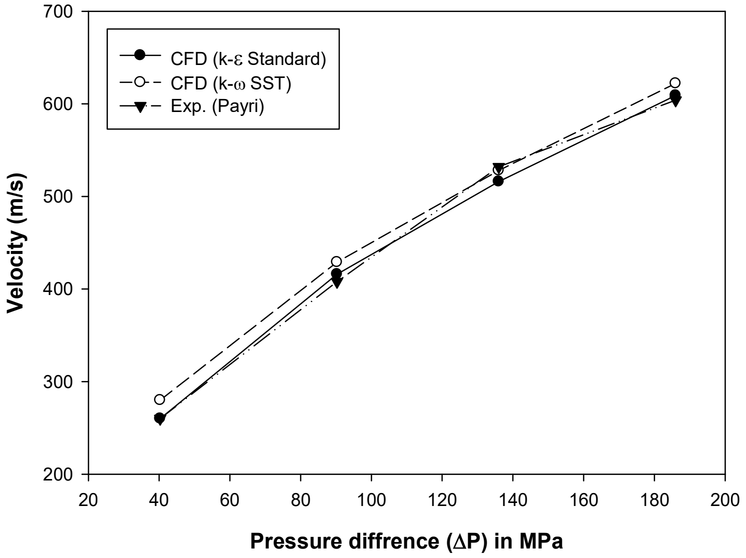

Fig 5.15 Outlet velocity at different combination of inlet and back pressure

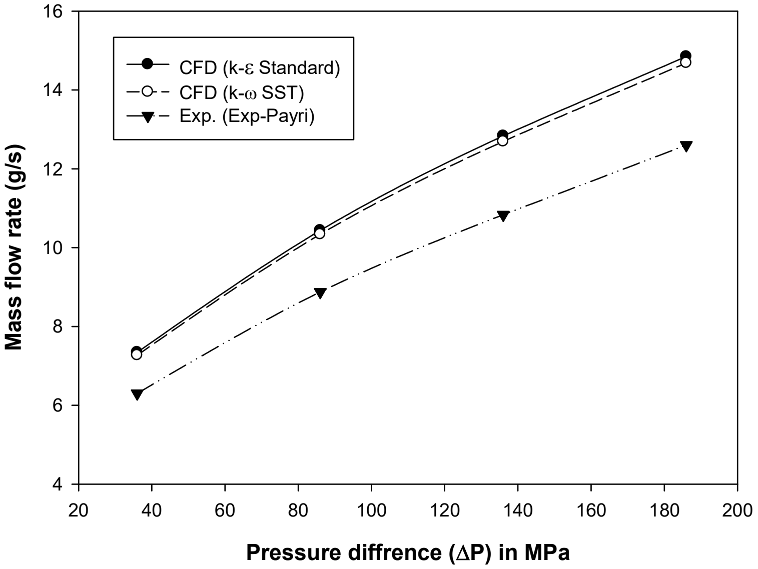

Fig 5.16 Mass flow rate at different combination of inlet and back pressure

Fig. 5.16 shows that the estimated mass flow rate is relatively high when compared to experimental data in both turbulence models. Because of the cavitating state, the effective diameter of the liquid phase at the nozzle exits decreases. This fact must consider while calculating the mass flow rate at the nozzle exit using CFD. With the help of volume fraction contour, we can calculate the effective outlet diameter which is listed in Table 5.3. It shows that as pressure difference increases effective diameter reduces from 212 mm to 176.3mm, these results are consistence with experimental findings.

Fig. 5.17 shows the comparison of effective outlet diameter with experimental calculations; it also demonstrates the method to determine effective diameter. Calculate the coefficient of diameter (D_{eff}/D_{out}) and multiply the obtained data by the k-ω turbulence model. The calculated mass flow rate matched the experimental values after adjustments shown in Fig 5.18. The diameter coefficient directly governs the area coefficient and discharge coefficient. Eventually, the discharge coefficient of the nozzle is reduced as cavitation flow develops inside the nozzle. However, this loss can be compensated by the advantages of cavitation flow on spray breakup.

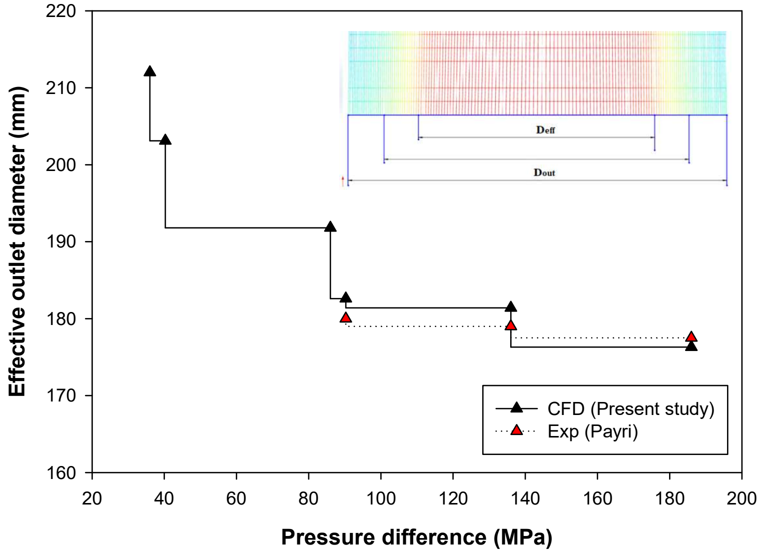

Fig. 5.17 Effective outlet diameter at different combination of inlet and back pressure

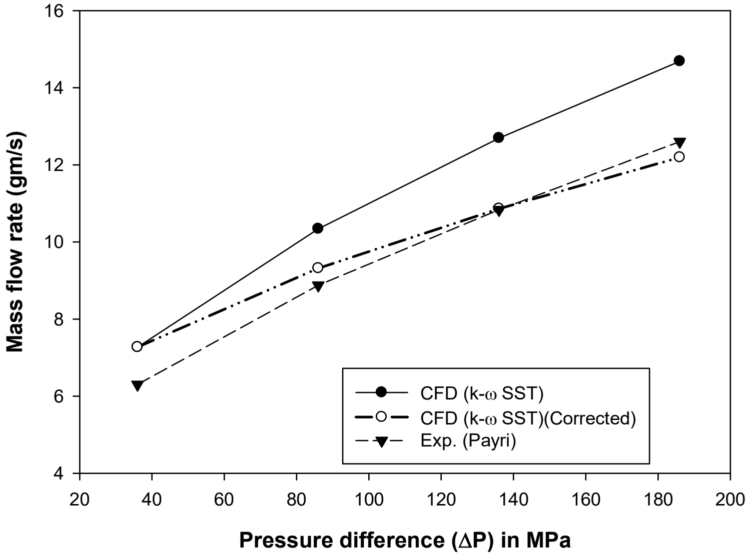

Fig 5.18 Corrected mass flow rate at different combination of inlet and back pressure

The pressure drop at the nozzle inlet increases with the pressure difference between the inlet and outlet. The reduction in static pressure in the throat is significant. When pressure drops below saturation pressure in the vena contract region, cavitation and phase change occur. As the pressure differential increases, so does the length of cavitation, signifying that cavitation propagates towards the exit.

Fig. 5.19 (a) shows the static pressure along the length profile with the k-ε model, while (b) shows the profile with the k-ω model. The graphic shows an almost flat line with zero static pressure for the majority of the nozzle length. This increases cavitation in the nozzle. The graph at the outlet shows an upward shift due to back pressure. The only profile on the chart that differs from the others is the 50-14 MPa example. Because the pressure differential between input and output pressures is small, the nozzle is less cavitating.

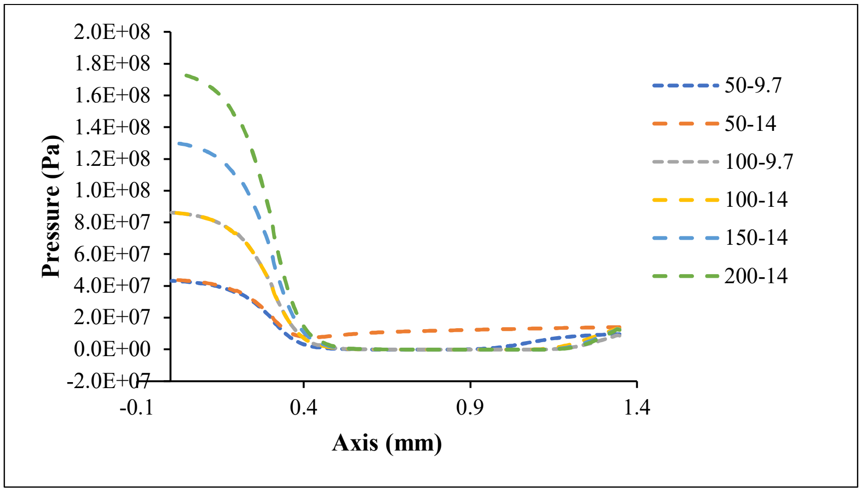

(a) k-ε turbulence model

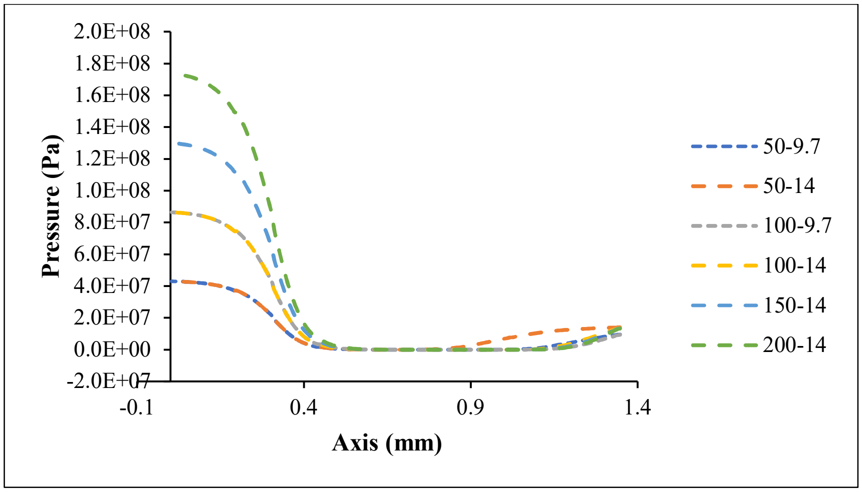

(b) k-ω turbulence model

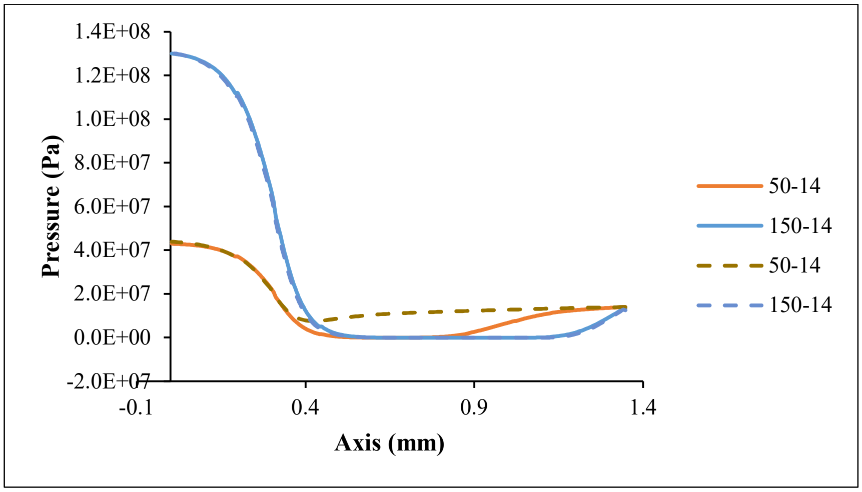

(c) comparison of k-ε and k-ωturbulence model

Fig 5.19 Static pressure distribution along the nozzle length

Figure 5.19 (c) shows a comparison of the profiles of both models. For this aim, we selected two cases. One is highly cavitating (150-14), whereas the other is less cavitating (50-14). To understand the difference between the two models, the model is represented by the full line and dashed line. For the 150-14 scenario, both models have nearly identical graph profiles. Cases 50-14 show a significant variation between the two model profiles. Due to these differences, k-ε shows the cavitation inception stage, while k-ω indicates the development of the cavitation stage in Fig 5.14.

(a) Profile data at Outlet of the nozzle

To conduct a quantitative analysis of the flow at the exit of a nozzle, we need to investigate a few variables at the nozzle's outlet. To understand the impact of parameters on spray breakup, we should develop the three profiles at the nozzle's exit, which include liquid fraction, turbulent kinetic energy, and velocity magnitude. Fig. 5.20 shows the liquid volume of fraction at the nozzle outlet using k-ε and k-ω turbulence model. The basic principle used in calculation is$f_l + f_v = 1$, where f_l and $f_v$are liquid fraction and vapor fraction. Fig. 5.20 (a) shows results with k-ε and (b) shows results with k-ω turbulence model. As the pressure difference increases, the liquid fraction near the nozzle wall reduces, implying that the vapor fraction near the wall rises. As the pressure between the inlet and outlet increases, the liquid fraction profile reduces significantly (vapor fraction increases). However, the profile does not decrease as strongly at a certain ΔP (150MPa-14MPa). Fig. 5.20 (a) and (b) show a larger vapor fraction as ΔP increases. The near-nozzle edge vapor proportion is approximately 40 to 50%. Figure 5.20 (c) compares profiles from two models. Because of the model's significant cavitation initiation, the k-ω profile has a higher vapor fraction than the k-ε turbulence model.

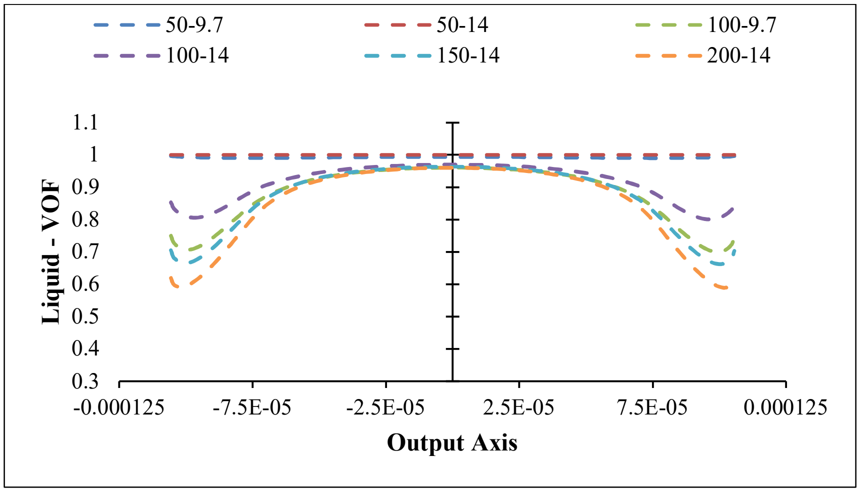

(a) Liquid-VOF profile at nozzle exit with k-ε model

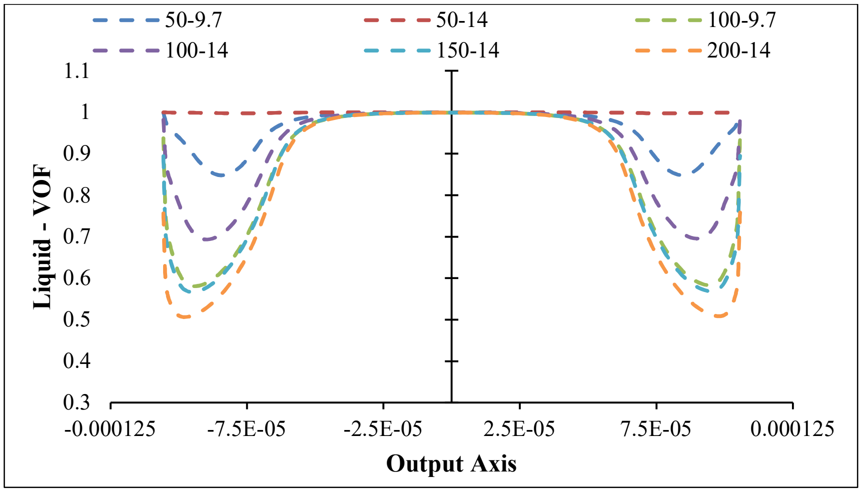

(b) Liquid-VOF profile at nozzle exit with k-ω model

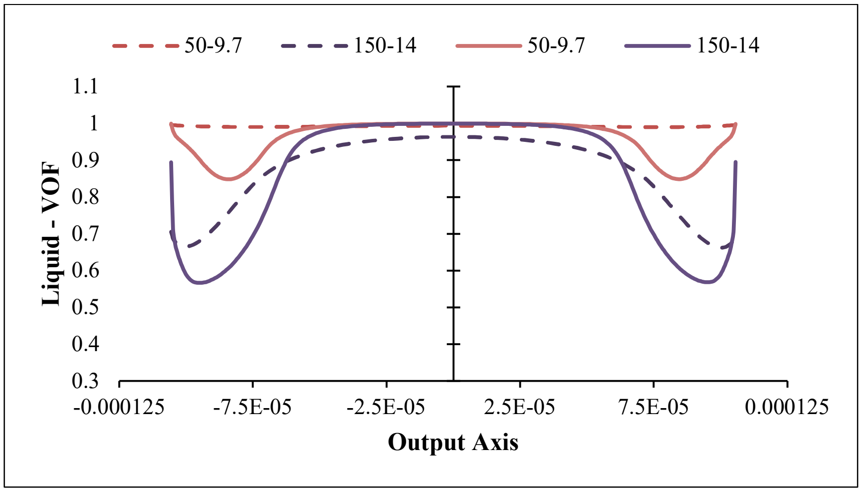

(c) Comparison of k-ε and k-ωturbulence model

Fig 5.20 Liquid volume of fraction profile at nozzle outlet

Fig. 5.21 shows the velocity profile at the outlet of the nozzle with different inlet and outlet pressures. Fig. 5.21(a) shows results derived using the k-ε model, while Fig. 5.21(b) shows results from the k-ω turbulence model. It shows that the maximum outlet velocity increases with a rise in pressure difference. Cavitation arises on both sides of the nozzle wall, reducing the effective velocity in that location. Fig. 5.21 (c) illustrates a comparison of two turbulence models. The velocity profile differs significantly between the k-ε and k-ω turbulence models with 50-9.7 pressure difference. The k-ε has no cavitation at the exit, while the k-ω has just mild cavitation.

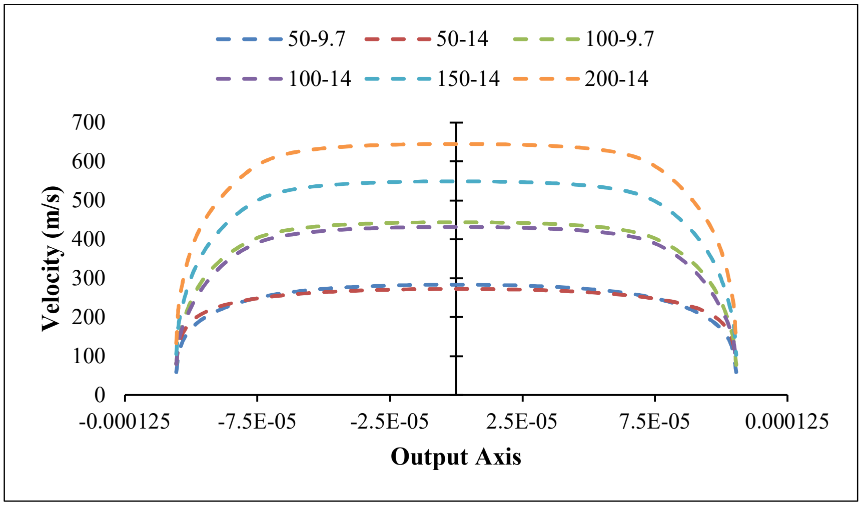

(a) Velocity profile at nozzle exit with k-ε model

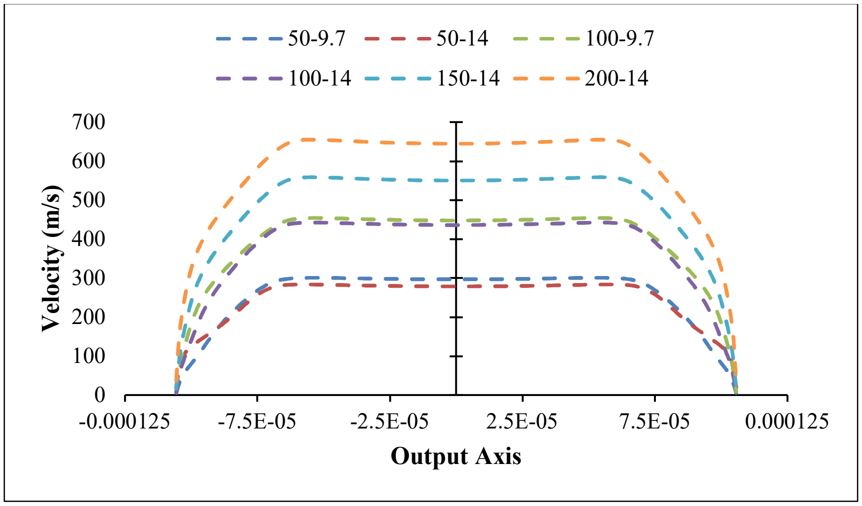

(b) Velocity profile at nozzle exit with k-ω model

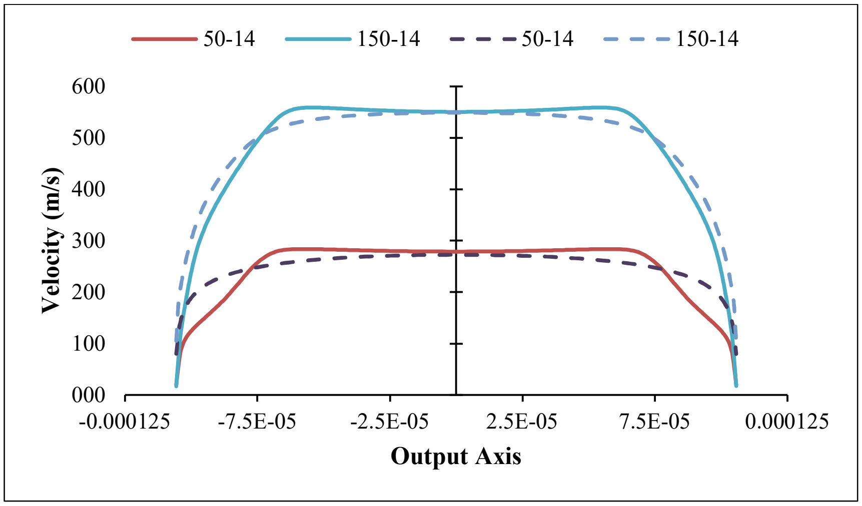

(c) Comparison of k-ε and k-ωturbulence model

Figure 5.21 Velocity profile at different inlet and outlet pressure

Turbulent kinetic energy (TKE) is extremely significant in spray breakup. Fig. 5.22 shows the computed TKE profile at the nozzle exit. The pressure differential has a substantial impact on the TKE profile. As the pressure difference increases, so does the TKE, particularly the peak value at the nozzle wall. The cavitation phenomenon is turbulent in nature, resulting in high TKE values near the wall. Interestingly, k-ε predicts higher values of TKE than k-ω for a given pressure difference. The TKE increases significantly from the non-cavitating instance (50-9.7) to the cavitating case (150-14), as illustrated in Fig. 5.22(c).

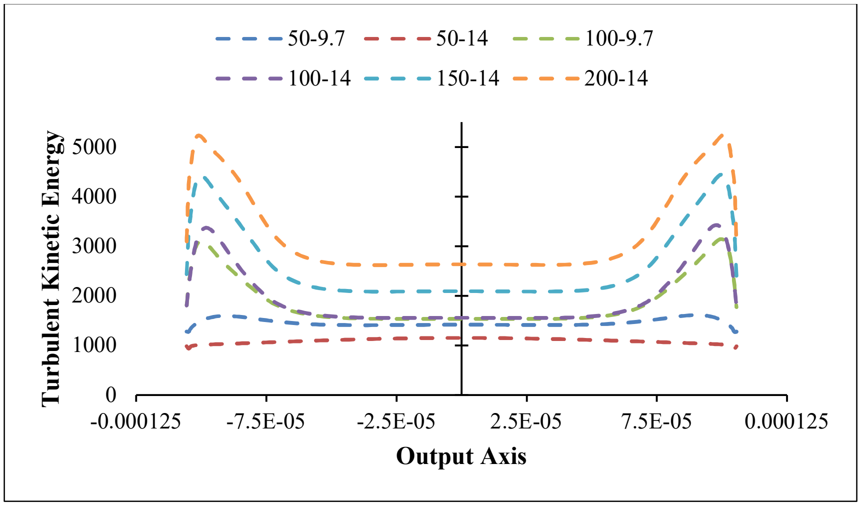

(a) TKE profile at nozzle exit with k-ε model

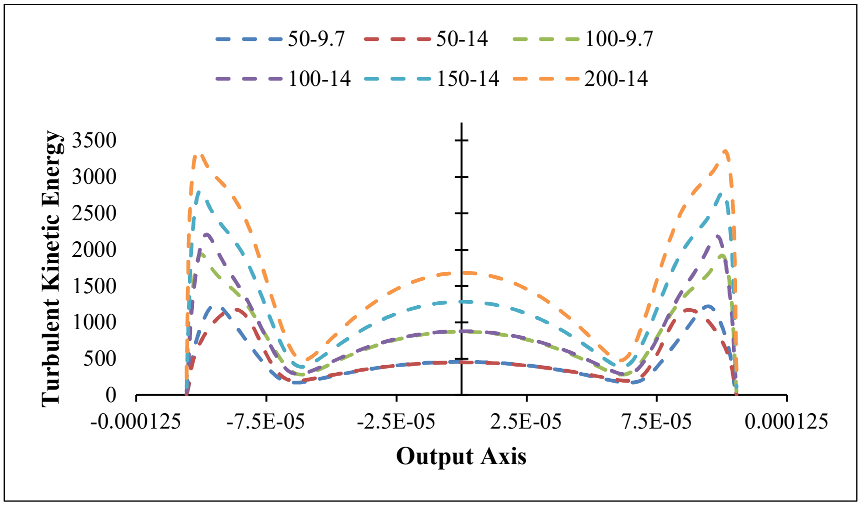

(b) TKE profile at nozzle exit with k-ω model

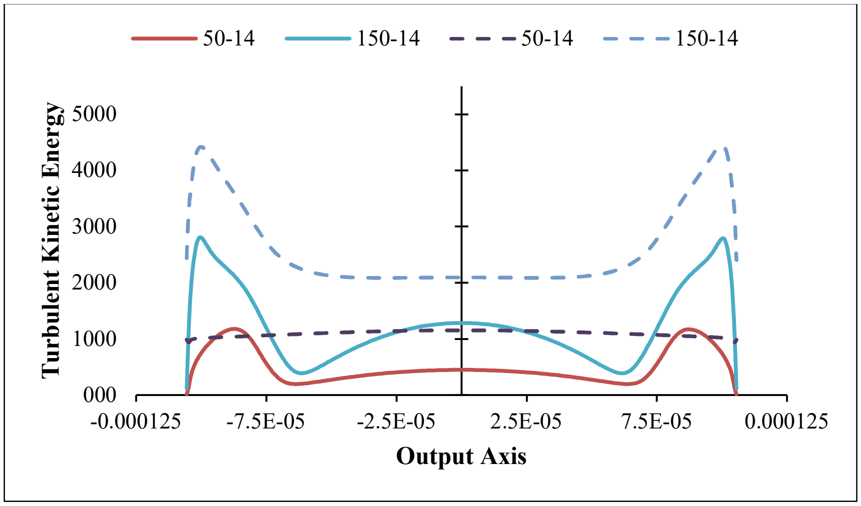

(c) Comparison of k-ε and k-ωturbulence model

Fig 5.22 Turbulent kinetic energy profile at different inlet and outlet pressure

(b) Spray breakup

As previously mentioned, we adopted a two-way coupling method, with the outlet parameters of internal flow assigned as an inlet for spray simulation. Spray simulations are performed using two turbulence models, similar to internal flow. Fig. 5.23 depicts the spray shape for the k-ε and k-ω turbulence models. The k-ε shows intermediate spray breakup, whereas the k-ω maintains the spray's conical shape. The total spray plume appears identical in both scenarios. There is no literature available to compare the present results.

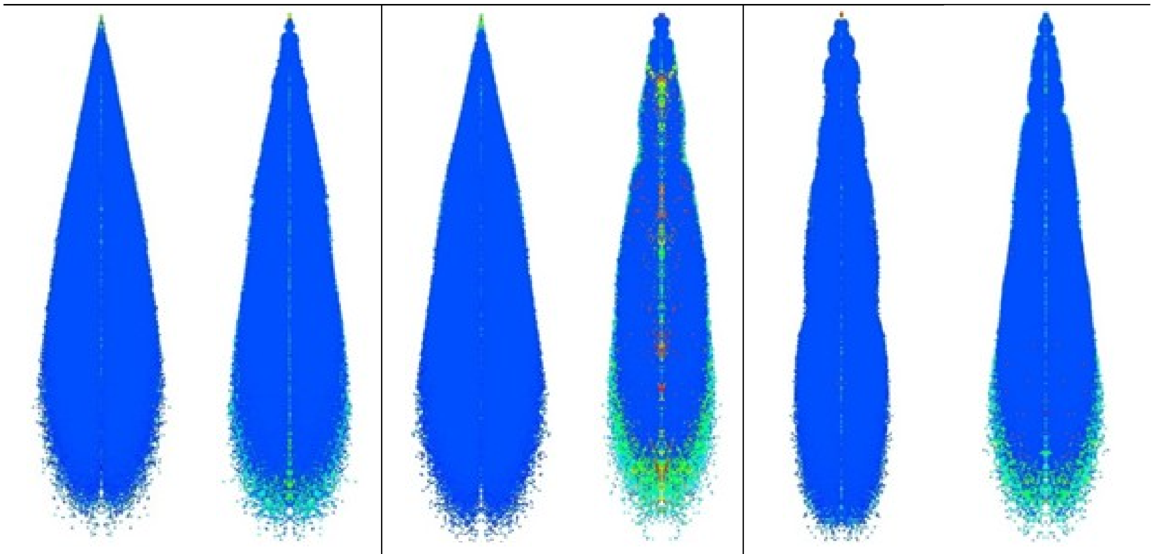

k-ε (Standard) k-ω (SST) P_{inj}= 50MPaP_{back}= 14MPa

k-ε (Standard) k-ω (SST) P_{inj}= 50MPaP_{back}= 9.7MPa

k-ε (Standard) k-ω (SST) P_{inj}= 100MPaP_{back}= 14MPa

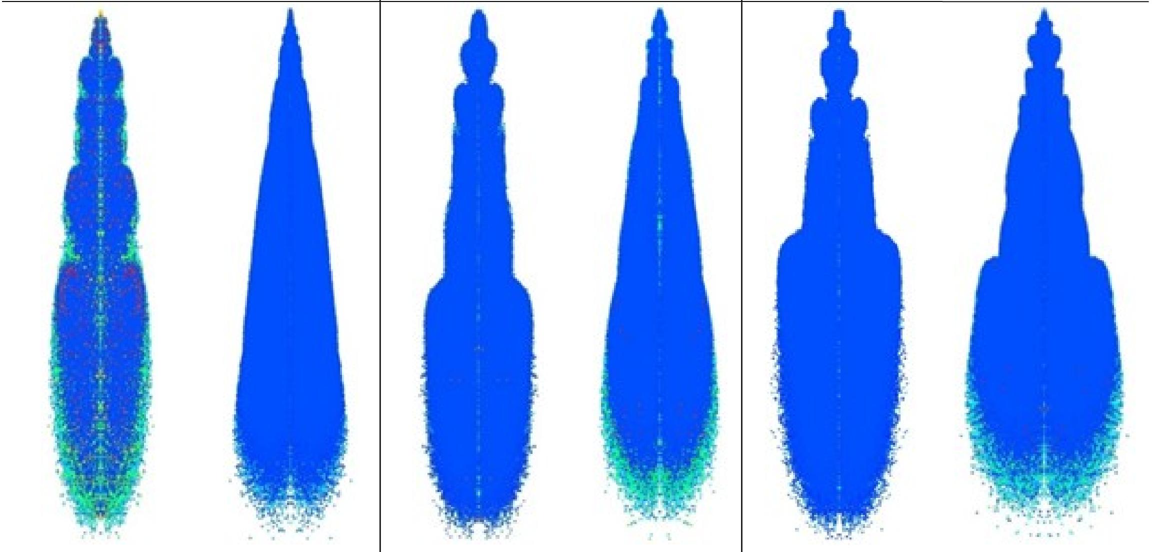

k-ε (Standard) k-ω (SST) P_{inj}= 100MPaP_{back}= 9.7MPa

k-ε (Standard) k-ω (SST) P_{inj}= 150MPaP_{back}= 14MPa

k-ε (Standard) k-ω (SST) P_{inj}= 200MPaP_{back}= 14MPa

Fig 5.23 Spray shape at different inlet and outlet pressure

(c) Cavitation induced spray breakup

As previously mentioned, we adopted a two-way coupled method, with the outlet parameters of internal flow assigned as an inlet for spray simulation in DPM model. The spray simulation is carried out only with k-ω SST turbulence model. The results are representing with reference to back pressure values of 14 MPa. It is found that, cavitation moves downstream as the pressure differential increases. The intensity of cavitation increases as the pressure difference between the input and output expands. The various stages of cavitation have been identified, as Fig. 5.24 illustrates. These stages include cavitation development (50-14 MPa) and super cavitation (150-14 MPa). The corresponding spray images were acquired using a two-step coupling method, revealing a noticeable increase in the cone angle during the super cavitation stage.

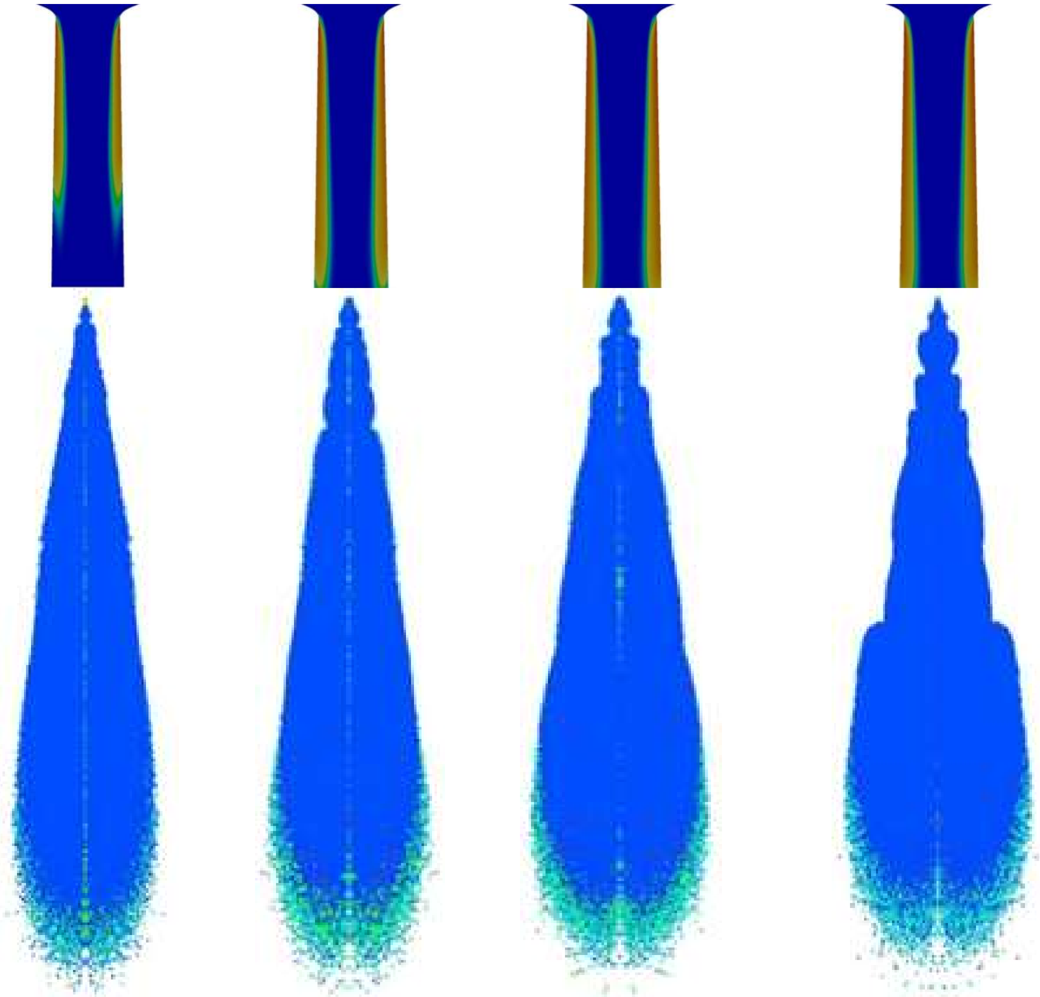

P_{inj}= 50 MPa - P_{back}= 14 MPa	P_{inj}= 100 MPa- P_{back}= 14 MPa	P_{inj}= 150MPa - P_{back}= 14MPa	P_{inj}= 200MPa- P_{back}= 14MPa
θ=15.8˚	θ=16.9˚	θ=19.8˚	θ=22.3˚

Fig 5.24 Cavitation coupled spray breakup

The spray breakup can understand by further investigation on the spray characteristics. The interaction with the entrained gas causes droplet velocities to be lowest in the radial and spray axis. In a dense spray, droplet collisions are very common. These collisions may cause changes in the size and velocity of the droplets. Drops can be divided into smaller ones. The Sauter mean diameter (SMD) is a measurement that describes the average droplet size of a spray and thus the effectiveness of spray breakup. The SMD is the diameter of a model drop with a volume-to-surface-area ratio equal to the sum of all droplet volumes in the spray divided by all droplet surfaces. The larger the surface area per unit volume, the lower the SMD. The larger the surface area, the more effective evaporation and mixture formation. Even though the SMD is a well-known statistic for characterizing the spray generation process, it is important to note that it does not include information about the spray's droplet size distribution. In other words, droplet size distributions across two sprays with the same SMD can differ greatly [4]. Numerous researchers have done and published studies looking at mean particle diameter (MPD) as a function of boundary conditions. Because the majority of the tests were conducted with quasi-stationary sprays, the data can only be used to represent the primary injection phase (full needle lift) of full-cone sprays [4]. Table 5.4 summarise the values of MPD and SMD at different inlet and outlet condition.

Table 5.4 Mean particle diameter (MPD) and Sauter mean diameter (SMD)

Sr. No.	Inlet - Outlet Pressure (MPa)	ΔP (MPa)	MPD ($\times 10^{-6}$ m)		SMD ($\times 10^{-6}$ m)	
			k-ε	k-ω	k-ε	k-ω
1	50-14	36	40.49	32.81	64.24	53.32
2	50-9.7	40.3	37.70	19.67	58.18	41.89
3	100-14	86	18.21	21.43	29.98	33.63
4	100-9.7	90.3	16.92	24.66	25.83	35.90
5	150-14	136	15.06	14.97	23.82	26.03
6	200-14	186	11.60	14.85	19.98	20.70

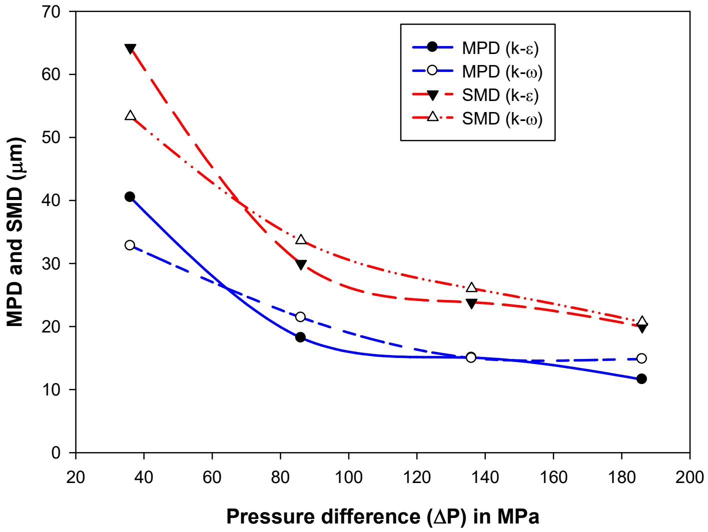

Fig. 5.25 MPD and SMD at different inlet and outlet pressure

Fig. 5.25 illustrates the computation of MPD and SMD at various injection pressures using the k-ε and k-ω turbulence models. The k-ε and k-ω predict almost identical results. The MPD and SMD decrease as injection pressure rises. The drop in SMD and MPD indicates that the spray chamber is operating under favourable conditions. The considerable drop in SMD and MPD seen at injection pressures of 150 and 200 MPa is consistent with the prior discussion. Super cavitation enhances both the spray cone angle and spray breakup (SMD and MPD). The two-step coupling method precisely calculates the influence of cavitation on the spray.

5.3 EXPERIMENTAL RESULTS OF SCALED UP NOZZLE

It is essential to validate numerical findings with experimental work. The objective of the present section is to demonstrate the capability of the nozzle, which has been designed to characterize the cavitation flow. The numerical simulation using the two-step coupling method indicates that the spray cone angle increases during the super cavitation, which needs to be verified using experimentation. It is very difficult to create visual access with a real-size nozzle, so the present work uses a scaled-up nozzle, and calculations are presents in forms of non-dimensional numbers. The experimental investigation was conducted with three different optical excess cavitation nozzles (CN 3, CN 4, CN 5) with three different fluids (Water, Diesel, Bio-Diesel). The cavitation nozzles operate with injection pressure ranging from 0.5 bar to 8 bar, revealing a diverse range of corresponding flow rates ranging from 3 to 8 litters per minute (LPM).

5.3.1 Results of cavitation nozzle 3 (CN 3)

(a) Water

The experimental investigation used a rectangular cross-section nozzle [width (Wn) = 5mm and depth (t) = 1mm, L/W=5]. The water passed through the nozzle at injection pressures ranging from 0.7 to 5.8 bars. High-speed cameras (up to 1000 frames per second) were used to take still images at different injection pressure levels. A suitable setup of the light source has been made to obtain a clear image. The photograph was acquired after flow and as the level of cavitation stabilized. The flow rates are controlled by a ball valve and a needle valve. There is no cavitation up to a flow rate of 4 LPM, which is classified as a no-cavitation stage. The cavitation bubbles were observed to commence at 1.5 bar injection pressure, indicating cavitation inception. The amplitude of cavitation bubbles rises as flow rate and pressure increase; this is referred to as cavitation development. Finally, bubbles reach the nozzle exit at an injection pressure of 4.1 bar, indicating the super cavitation stage. Further pressure rises resulted in a hydraulic flip stage at 5.4 bar as shown in Fig 5.26. This visual representation offers a concise overview of the observed phenomena and their dependencies within the tested nozzle configuration. This cavitation map shows all distinct stages of cavitation, i.e. inception of cavitation, growth of cavitation, super cavitation, and hydraulic flip.

ΔP= 1.5 bar	ΔP= 2 bar	ΔP= 3 bar	ΔP= 4.1 bar	ΔP= 5.4 bar
Cavitation Inception	Growth of Cavitation	Growth of Cavitation	Super cavitation	Hydraulic Flip
θ = 5.1˚	θ =6.7˚	θ =10.7˚	θ =12.9	θ =7.7˚

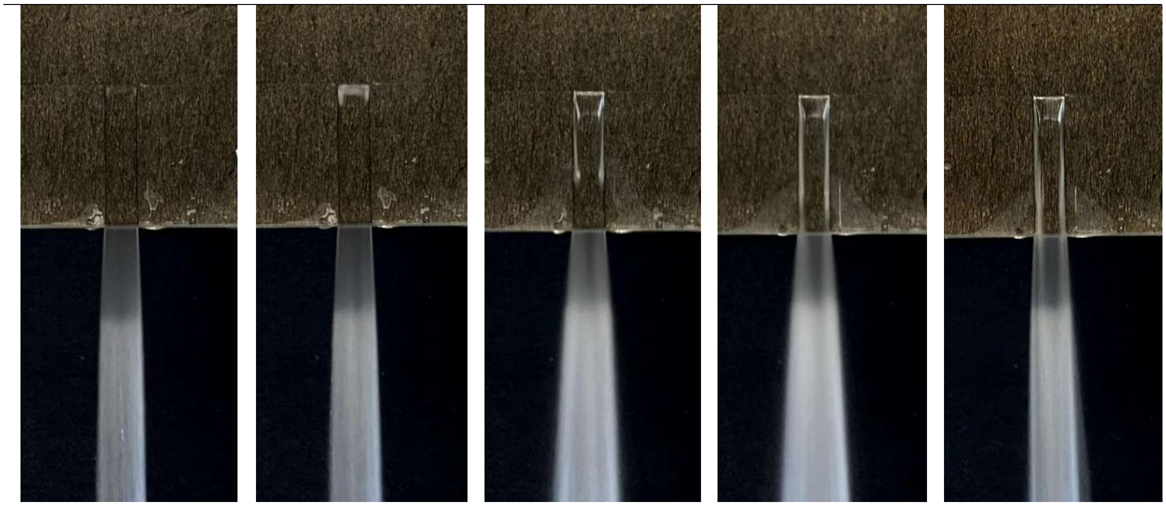

Fig 5.26 Different cavitation stages coupled with spray results with scaled up nozzle (CN 3)

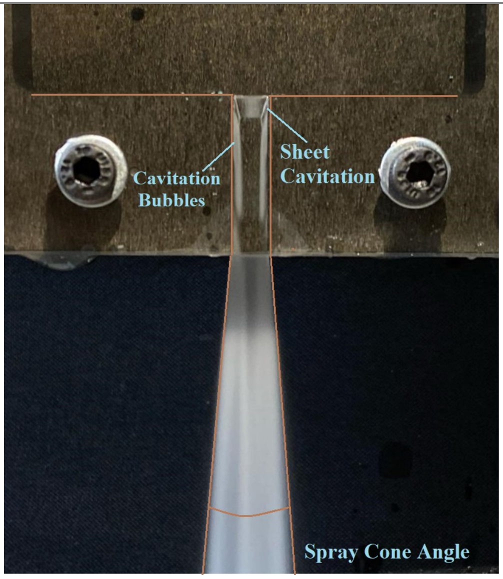

Fig. 5.27 Actual image of cavitation bubbles and sheet cavitation inside the nozzle

Despite having a minimal depth of 1 mm, this nozzle is rightly referred to as '3D' owing to its reservoir's distinctive three-dimensional shape. The reservoir's unique geometry plays a crucial role in influencing cavitation formation from a third direction, thereby observed a novel sheet type cavitation phenomenon, which was observed in the inception stage up to hydraulic flip, a worth mentioning finding of cavitation characteristics shown in Fig.5.27.

The primary goal of the current research is to investigate cavitation flow and its effect on spray characteristics. The cavitation flow, among other spray properties, has a considerable effect on the spray cone angle. The spray cone angle is estimated based on the liquid edge's divergence from the vertical line. The spray cone angle increases with increasing injection pressure. The highest spray cone angle was observed during super cavitation, as shown in Fig. 5.28. During super cavitation, vapor bubbles collapse at the nozzle output. The liquid jet will encounter turbulence as a result, which will improve the breakup mechanism. Hydraulic flip occurs when there is an additional increase in injection pressure, which causes air entrainment inside the nozzle and flow separation from the nozzle surface. Hydraulic flip reduces the spray cone angle.

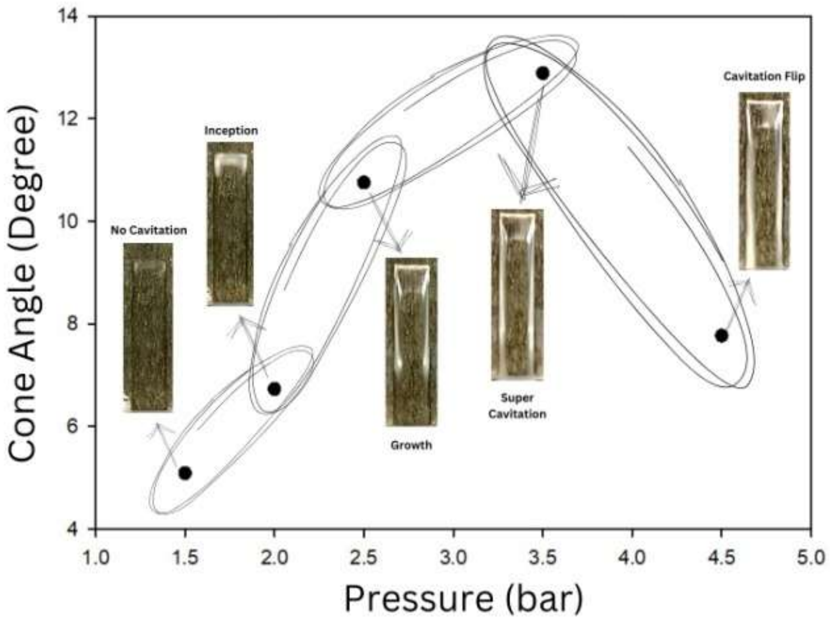

Fig 5.28 Spray cone angle vs. Injection pressure (CN 3W)

Due to visual restrictions, the scaled-up nozzle was used in the current study. It is critical to maintain geometric, kinematic, and dynamic similarities between scaled-up and real-scale nozzles. To characterize the cavitation flow and spray breakup, non-dimensional numbers such as the Reynolds number, discharge coefficient, and cavitation number are calculated from experimental data. These non-dimensional numbers were calculated using the following equations:

Reynolds number:
$$Re = \frac{\rho V D_h}{\mu} \tag{5.6}$$

Discharge coefficient:
$$C_d = \frac{\dot{m}_{actual}}{A\sqrt{\frac{2\Delta P}{\rho}}} \tag{5.7}$$

Cavitation number:
$$CN = \frac{P_{back} - P_v}{{}^1/_2\, \rho V^2} \tag{5.8}$$

In which ρ density of liquid, V is the velocity at the outlet of the nozzle, D_h hydraulic diameter, ΔP difference between injection and back pressure, P_{back} is the outlet or atmospheric pressure, P_v is the vapour pressure of the liquid.

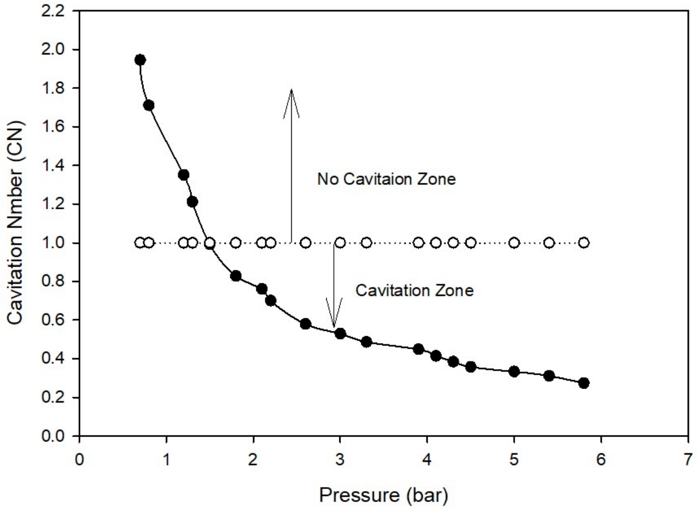

Fig 5.29 Injection pressure vs. Cavitation number (CN 3W)

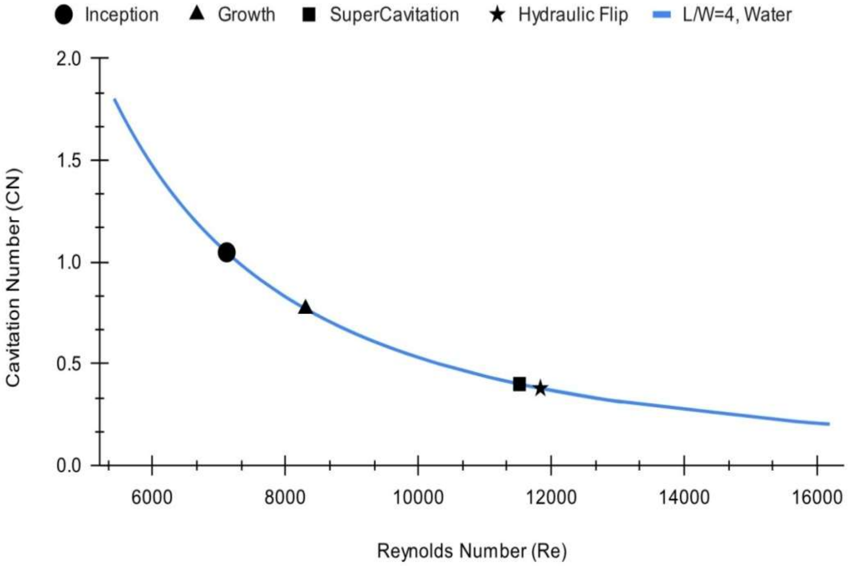

Fig 5.30 Reynolds number vs. Cavitation number (CN 3W)

According to equation 5.8, as the injection pressure increases, so does the velocity at the nozzle's outflow, lowering the cavitation number. Before the commencement of cavitation, there is a significant drop in CN, indicating a rapid decrease, as illustrated in Fig. 5.29. As CN approaches unity, cavitation begins, and the rate of CN reduction changes. The rate of CN reduction fluctuates as cavitation progresses, and the CN curve becomes asymptotic when the hydraulic flip occurs. Fig. 5.30 demonstrates similar behaviour to Fig. 5.29. The Reynolds number is directly proportional to velocity and injection pressure.

The size of the cavitation bubbles and cavitation region depends on the injection pressure or cavitation number. Fig. 5.31 presents a graph depicting the relationship between cavitation number and the characteristic length (Lc/L), where Lc represents the length of the cavitation zone and L represents the length of the nozzle. The graph illustrates an increase in the characteristic length as the cavitation number (CN) decreases. This trend aligns with expectations, as a decrease in CN signifies the initiation of cavitation formation. As a result, the cavitation zone length increases, as seen by the observed association in the chart. According to Akira Sou et al. [16], when the characteristic length approaches 0.70 to 1, it indicates the transition to the super cavitation stage. As the characteristic length approaches 1, the probabilities of transitioning from super cavitation to hydraulic flip increases. As a result, for persistent super cavitation, it is critical to keep the characteristic length between 0.8 and 0.9.

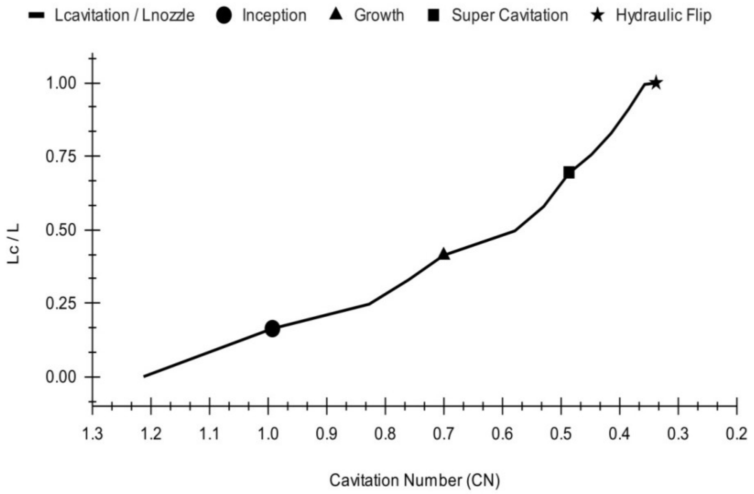

Fig 5.31 Cavitation number vs Characteristics length (Lc/L)

The efficiency of the nozzle is represented by the discharge coefficient (C_d), which is the ratio between the actual flow rate and the theoretical flow rate at a given pressure difference. When cavitation forms inside the nozzle, it reduces the nozzle's effective area, lowering the flow rate. During the hydraulic flip, external air enters the void between the orifice wall and the fluid inside the nozzle. This leads to a reduction in the effective exit cross-sectional area and a sudden drop in the discharge coefficient, as shown in Fig. 5.32.

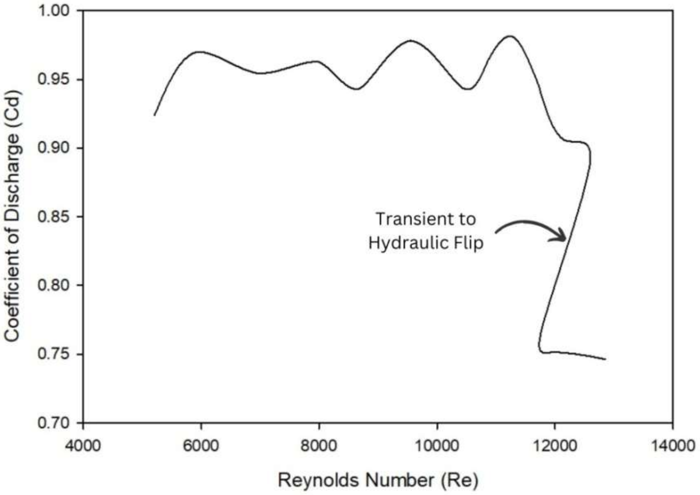

Fig. 5.32 Reynolds number vs Coefficient of discharge (CN 3W)

Main objective of current study is to find out effect of inner nozzle cavitation on the spray characteristics. It is evident that, during the super cavitation the wider spray appears. Fig. 5.33 explores the correlation between spray cone angle and Reynolds number, providing insights into the impact of cavitation on spray characteristics. The spray cone angle serves as a crucial indicator of cavitation effects on the spray pattern. The graph reveals a distinct trend: initially, at lower Reynolds numbers corresponding to low injection pressure, the spray cone angle is minimal. The cone angle increases linearly with Reynolds number and reaches its maximum value (θ=12.9˚) at super cavitation. Curves then begin to decrease because of hydraulic flips.

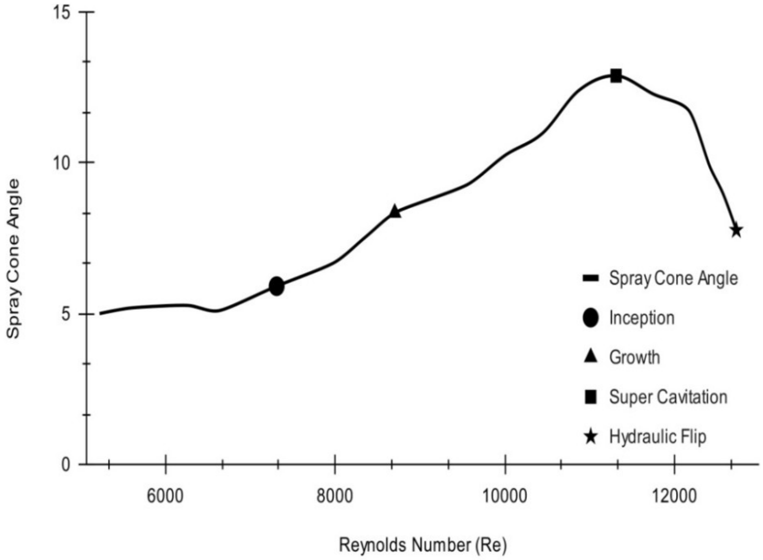

Fig. 5.33 Reynolds number vs Spay cone angle (CN 3W)

(b) Diesel

The study expanded to include diesel fuel. The studies were conducted with diesel fuel. The flow rate of diesel is increased by using a ball valve and a needle valve, which raise the pressure. The experiment effectively detected many stages of cavitation, including cavitation inception, growth, super cavitation, and hydraulic flip, as illustrated in Fig. 5.34. The cavitation impact on the spray cone angle is comparable to that seen with water. The highest cone angle measured during super cavitation.

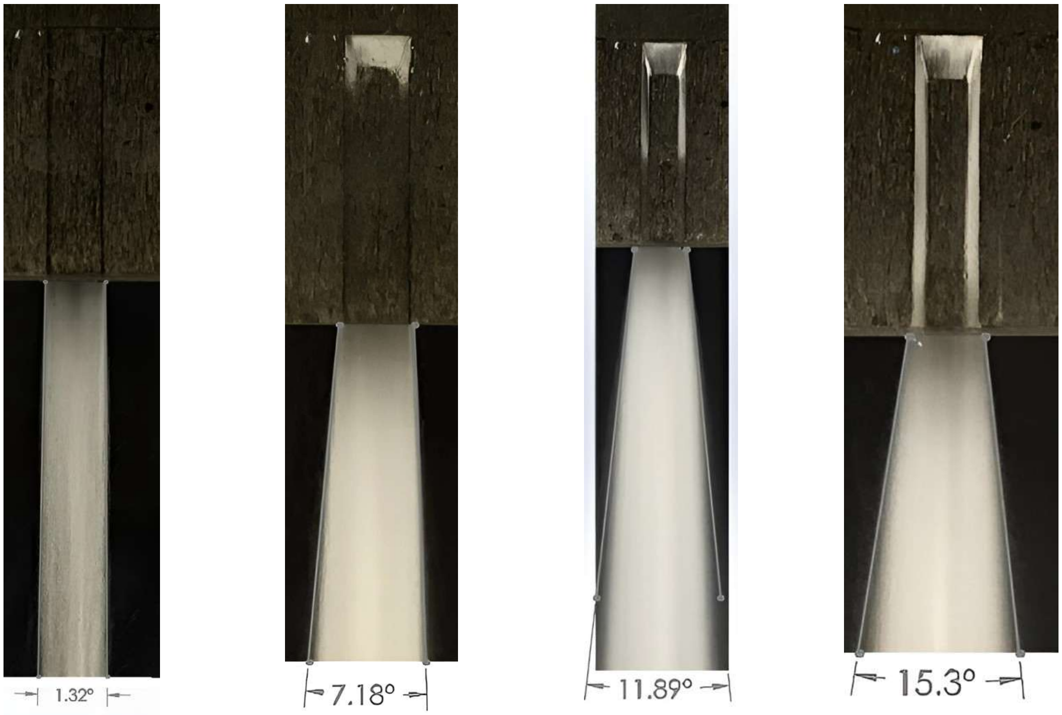

No cavitation

Inception of cavitation

Growth of cavitation

Supercavitation

Fig. 5.34 Different stages of the cavitation for diesel fuel

Fig. 5.35 depicts the volume flow rate relative to pressure for water and diesel. Because of its lower density, diesel fuel has a larger volume flow rate at a given pressure than water does. The cavitation flip causes sudden decreases in water and diesel flow rates. Diesel fuels have an earlier hydraulic flip than water. The findings for water and diesel are compared using non-dimensional numbers. Fig. 5.36 depicts the relationship between the Reynolds number and the cavitation number. The cavitation number drops with the Reynolds number because CN is inversely proportional to velocity. Fig 5.36 mentions the different stages of cavitation. Cavitation in water and diesel begins as the CN number approaches unity. Diesel demonstrates inception and super cavitation at substantially lower Reynolds numbers than water.

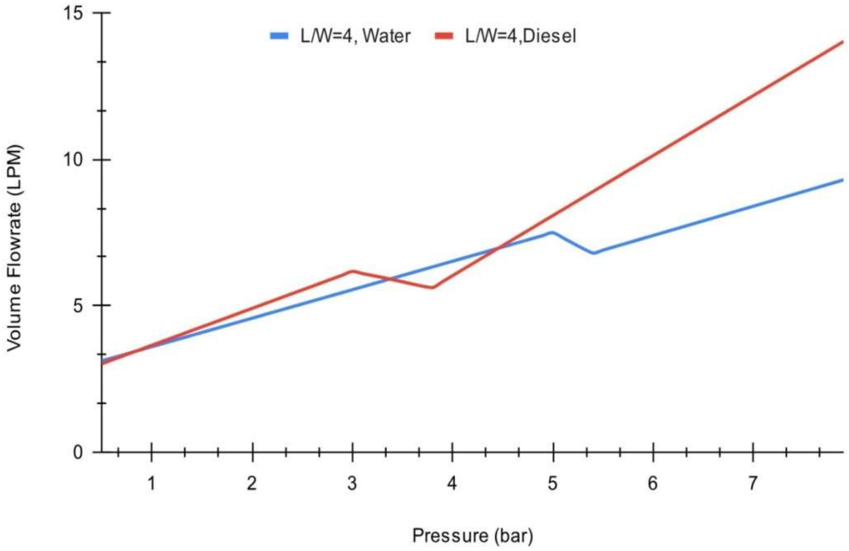

Fig 5.35 Pressure vs volume flow rate for water and diesel (CN 3WD)

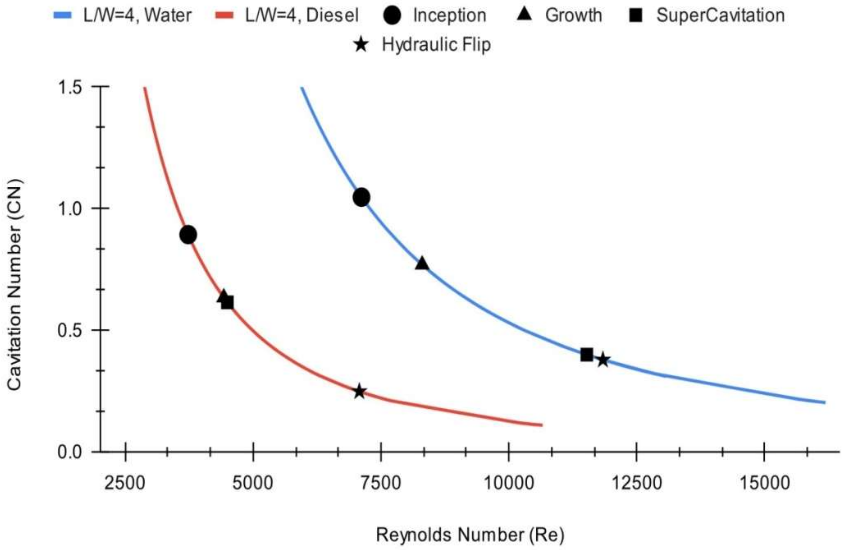

Fig 5.36 Reynolds number vs Cavitation number for Water and diesel (CN 3WD**)**

5.3.2 Results of cavitation nozzle 4 (CN 4)

The spray cone angle is determined by the spray breakup mechanism. The aerodynamic force and turbulence cause instability within the jet, and ligaments begin to form. When injection pressure is increased, the outlet velocity increases, resulting in more aerodynamic drag and improved spray breakup. Another possibility is to raise the turbulence intensity at the nozzle outlet. Cavitation bubbles collapse at the nozzle output, adding turbulent energy and improving spray breakup. The previous section concluded that the spray cone angle could increase during the super cavitation stage. Super cavitation happens under relatively high pressure. The increase in spray angle could be attributed to either increased velocity (aerodynamic drag) or increased turbulence (cavitation). One should find the actual. One should investigate the true cause of the spray cone angle improvement. The purpose of creating another cavitation nozzle 4 (CN 4) is to determine how super cavitation influences the spray angle. Before fabricating the nozzle, CFD study was performed using a shorter nozzle length on one side than the other. Fig. 5.37 shows the geometry, mesh and boundary conditions. The simulation was carried out to ensure that super cavitation occurs on one side of the nozzle. Fig. 5.38 depicts the pressure, velocity, and volume fraction of vapor at injection pressures of 3 bar, 5 bar, and 7 bar.

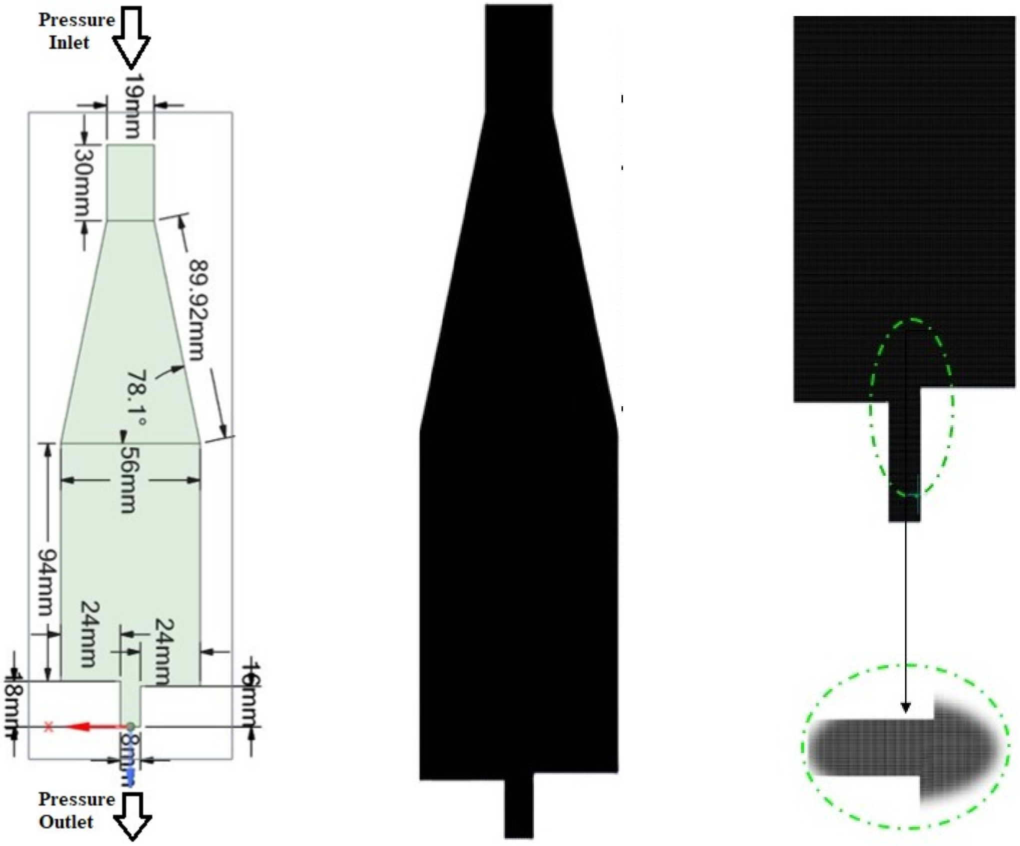

Fig. 5.37 Geometry, boundary condition and mesh details.

To calculate the nozzle length, a numerical simulation was performed. This assures that only one side of the nozzle experiences super cavitation flow, while the other side must operate under non-cavitation conditions. The pressure contours indicate negative pressure on the left side of the nozzle wall. The velocity contour reveals a significant flow separation on the left side vs the right-side wall. This will produce more vapor bubbles on the left side. Fig. 5.38 demonstrates how the nozzle's left side exhibits super cavitation, whereas the nozzle's right side exhibits non-cavitation flow due to a variation in nozzle height.

P_{inj}=3 bar P_{inj}=5 bar P_{inj}=7 bar

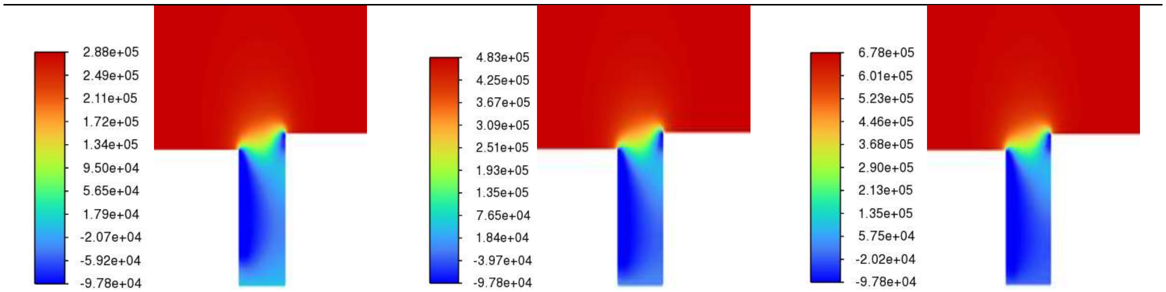

Static pressure contour

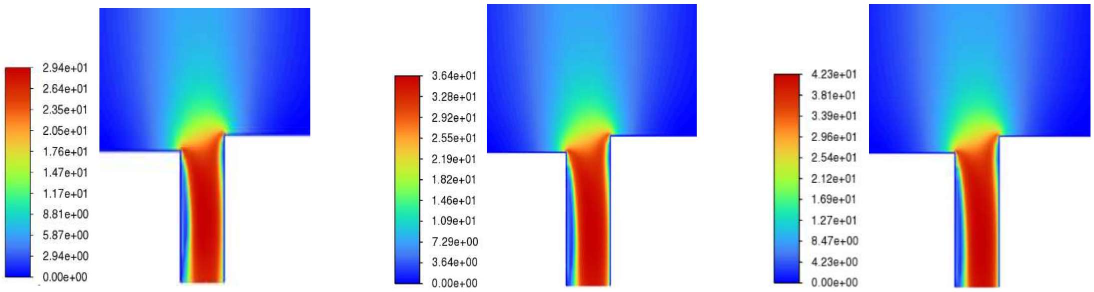

Velocity contour

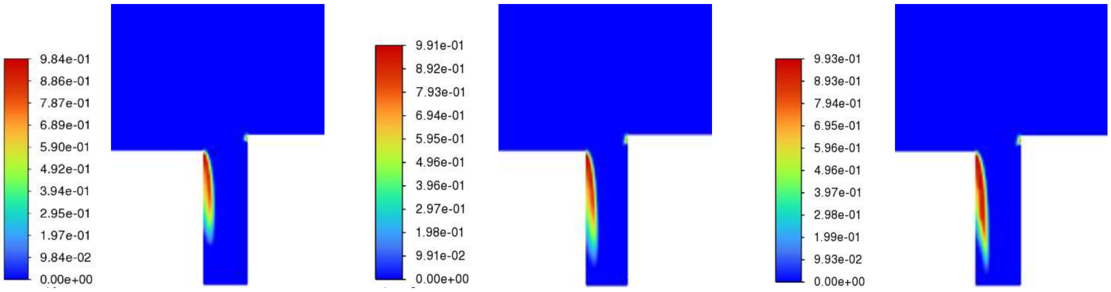

Volume fraction of vapor

Fig. 5.38 Pressure, velocity and vapour fraction contour for CN 4

Water, P_{inj}= 4.9 bar, θ=7˚ Diesel, P_{inj}= 6.6 bar, θ=11˚

Fig 5.39 Experimental results for CN 4 using water and diesel

Based on these findings, a similar-sized nozzle was fabricated. The experiment was carried out to demonstrate the influence of super cavitation on the spray angle using water and diesel fuel. Fig. 5.39 shows the results for water and diesel. The intensity of cavitation matches closely with the CFD data. Only one side of cavitation appears namely super cavitation. The water and diesel fuel spray image clearly shows a larger spray on the super cavitation side. This proves that super cavitation alone is responsible for the increased cone angle.

5.3.3 Results of cavitation nozzle 5 (CN 5)

The previous section used a rectangular cross-section nozzle, whereas genuine fuel injector nozzles are cylindrical in shape. The cylindrical nozzle was made of acrylic block to imitate the real-world situation as shown in Fig. 5.40. Sufficient care has been taken to ensure the acrylic nozzle is not damaged during the high operating pressure. This section highlights the experimental results using water, diesel, and WCO-based biodiesel. Qualitative and quantitative findings were collected to assess the effect of cavitation on spray breakup. For cross-validation, a CFD simulation of inner nozzle flow was performed and compared to experimental data. Fig. 5.41 depicts high-quality images of various stages of cavitation flow inside the acrylic nozzle. When the pressure increases, the fluid accelerates within the cylindrical nozzle. The cavitation bubbles appear surrounding the nozzle inlet. As pressure builds, cavitation bubbles form and flow downstream along the nozzle wall. The acrylic nozzle creates a three-dimensional flow effect and replicates the fluid behaviour of the bubbles inside the nozzle. The various stages of cavitation are compared for water, diesel, and WCO-based biodiesel.

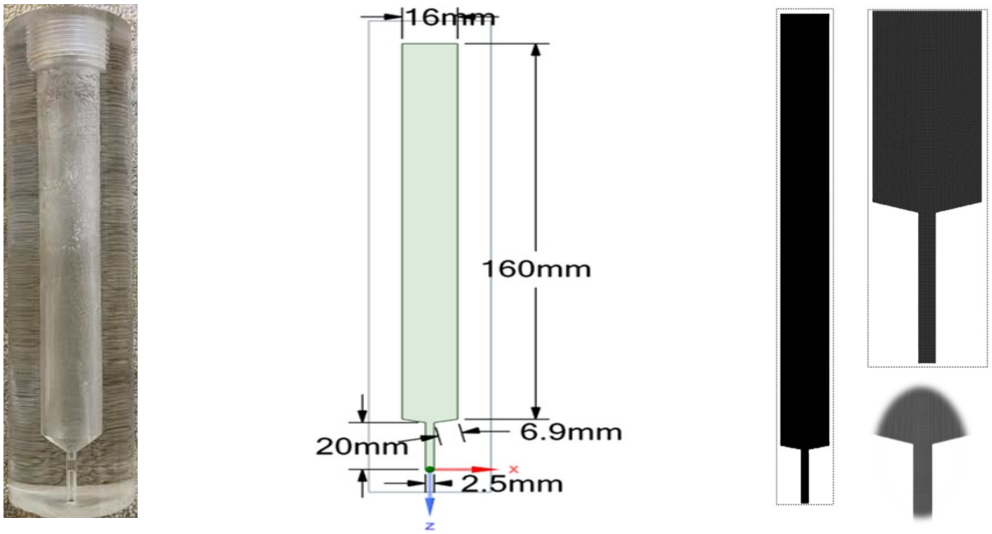

Acrylic nozzle (CN 5) Geometrical dimensions Mesh details

Fig. 5.40 Acrylic nozzle with its dimension and mesh details

No Cavitation	Inception of Cavitation	Growth of Cavitation	Super cavitation	Hydraulic Flip

Water

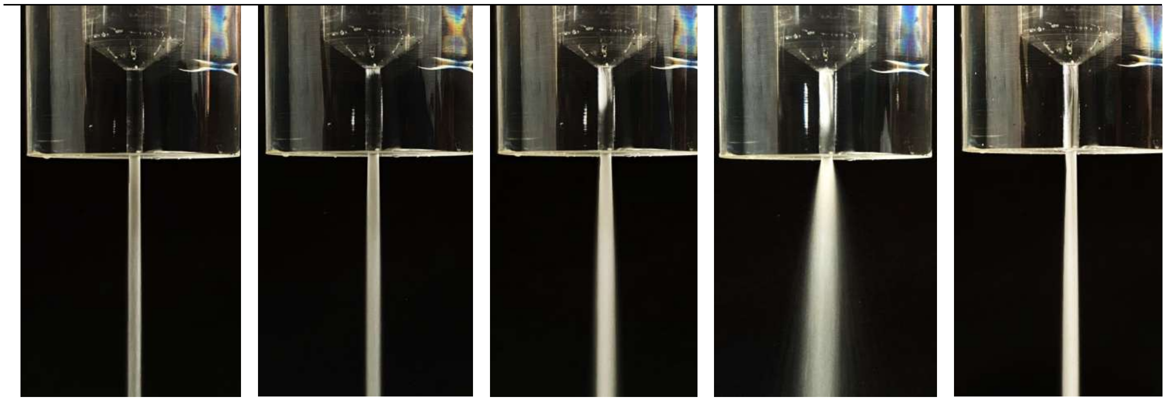

ΔP= 1 bar $\theta = 2.8^\circ$	ΔP= 1.7 bar $\theta = 3.3^\circ$	ΔP= 2.3 bar $\theta = 4.9^\circ$	ΔP= 2.6 bar $\theta = 17.6^\circ$	ΔP= 5.1 bar $\theta = 2.3^\circ$

Diesel

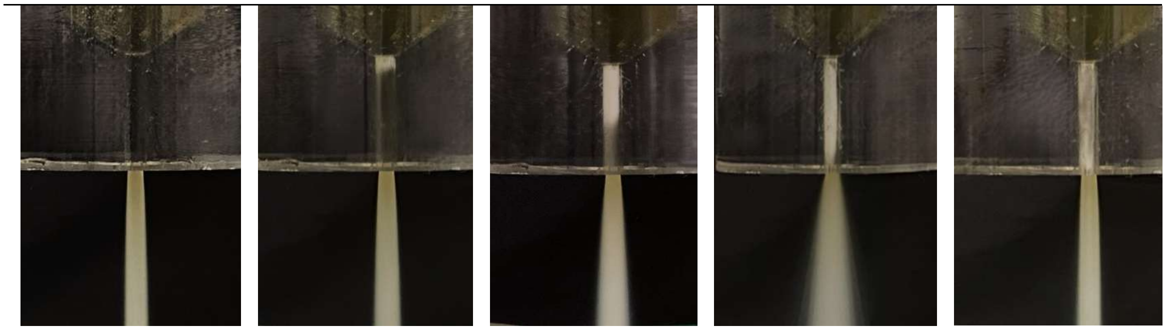

ΔP= 1 bar $\theta = 2.7^\circ$	ΔP= 1.8 bar $\theta = 4.5^\circ$	ΔP= 2.4 bar $\theta = 6.7^\circ$	ΔP= 2.9 bar $\theta = 12.3^\circ$	ΔP= 5.5 bar $\theta = 2.9^\circ$

WCO based bio-diesel

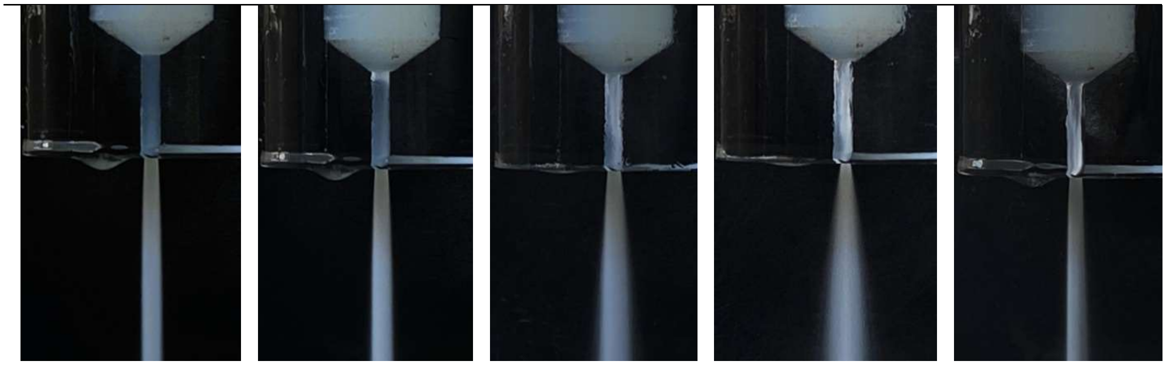

ΔP= 1 bar $\theta = 2.1^\circ$	ΔP= 2.2 bar $\theta = 2.9^\circ$	ΔP= 2.6 bar $\theta = 5.7^\circ$	ΔP= 3.1 bar $\theta = 9.8^\circ$	ΔP= 5 bar $\theta = 2.5^\circ$

Fig 5.41 Different cavitation stages coupled with spray results with scaled up nozzle

The current study aims to investigate the effects of inner nozzle cavitation and spray generation. It is critical to develop a solution for poor atomization characteristics of biodiesel due to its high viscosity. The atomization of any fuel can be improved by increasing the fuel spray angle. To determine the spray angle, utilize the angle formed by tangent lines going through the nozzle tip and along the spray surface in the "steady" area. Fig. 5.42 (a) depicts the spray cone angle relative to injection pressure. As described in the previous section, the above results suggest that the super cavitation stage generates the highest spray cone angle.

The highest cone angle during the super cavitation is observed with water and is followed by diesel and bio-diesel. Because water has the lowest viscosity, it produces a larger spray. Super cavitation improves the spray angle of WCO-based bio-diesel by about 4˚ (5.7˚ to 9.8˚). Super cavitation refers to the circumstance in which cavitation bubbles are about to evacuate the nozzle length. It is important to determine the non-dimension characteristic length at various pressures, as seen in Fig. 5.42 (b). The results demonstrate that the biodiesel required higher injection pressure to achieve a Lc/L of 0.7. Figure 5.42 (c) indicates the variation in volume flow rate with pressure. The flow rate increases linearly with pressure, however, due to cavitation, this trend is not observed in the current investigation. When pressure reaches a certain level, a hydraulic flip happens. Due to hydraulic flip caused by air entrainment, fluid separates from the nozzle wall, and flow becomes annual. This will dramatically lower the effective area and the volume of fluid that goes through it. Temporary reductions in the volume flow rates of water, fuel, and biodiesel are noticed. A further increase in pressure pushes the air within the nozzle, and the flow rate increases linearly with pressure.

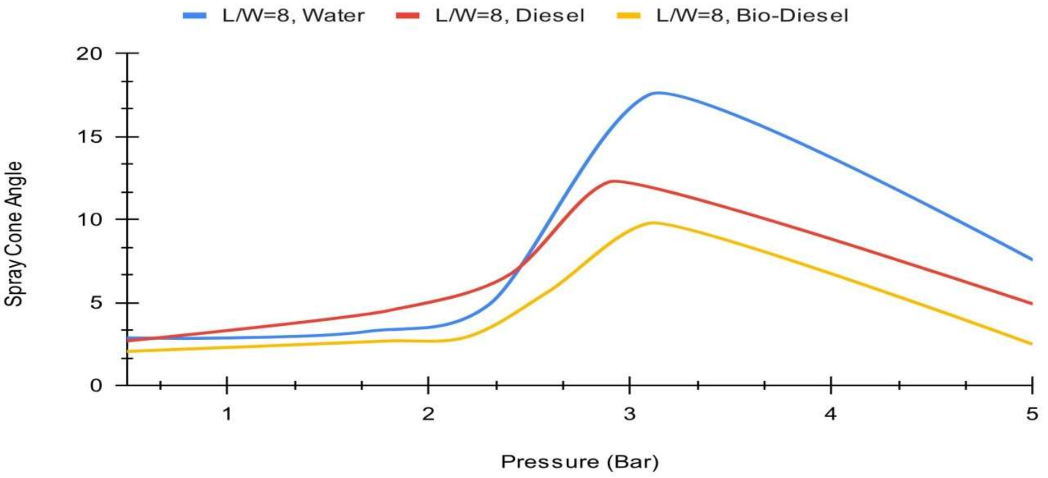

(a) Pressure vs Spray cone angle

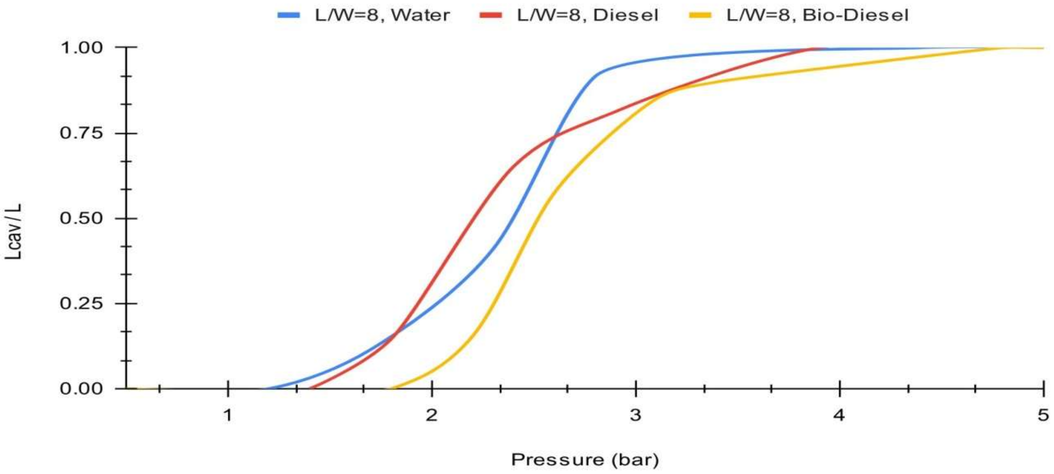

(b) Pressure vs Characteristic length

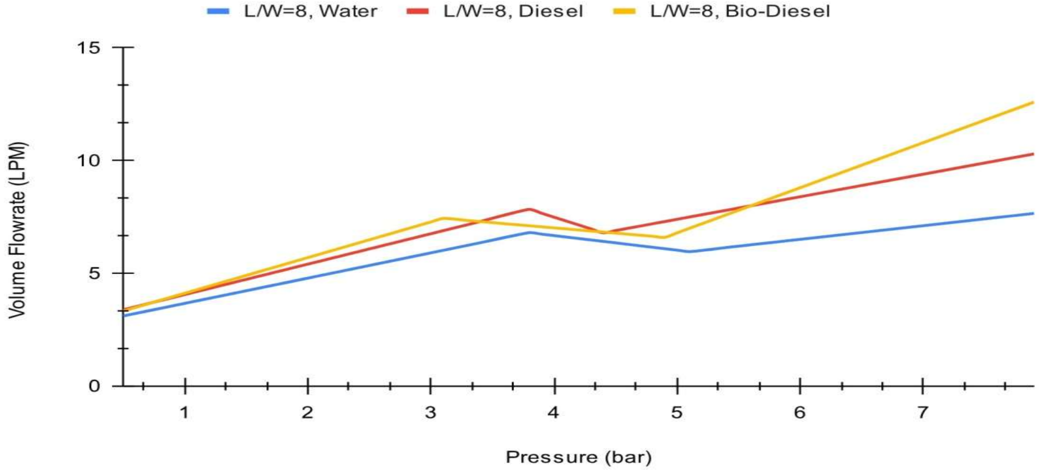

(c) Pressure vs Volume flow rate

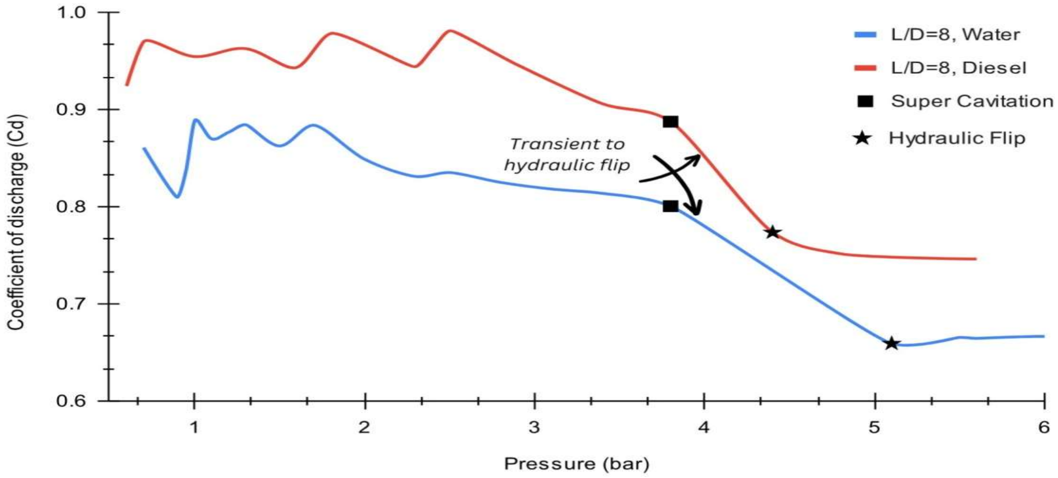

(d) Pressure vs coefficient of discharge

Fig 5.42 Effect of pressure on (a) Volume flow rate (b) Spray cone angle (c) L_{cav}/L (d) C_d

This behaviour was also seen when computing the discharge coefficient. As cavitation bubbles form inside the nozzle, the discharge coefficient begins to decline due to reduction in the effective area. The discharge coefficient decreases dramatically during the hydraulic flip, as illustrated in Fig. 5.42 (d). The magnitude of the discharge coefficient in the case of water is much lower than that of diesel fuel. The void generated inside the water flow had a bigger cross-sectional area than the diesel flow during cavitation.

Fig. 5.43 illustrates the spray cone angle at different Reynolds numbers. The Reynolds number is greatly affected by fluid properties. The Reynolds number is inversely proportional to fluid viscosity. Higher viscosity results in a lower Reynolds number. The WCO-biodiesel has a higher viscosity than the other; hence cavitation appears at a lower Reynolds number when compared to water and diesel. Although the same viscosity resistance persists, the spray breakup exhibits a smaller peak spray cone angle, as illustrated in Fig. 5.43. The maximum cone angle was recorded during super cavitation with water fluid.

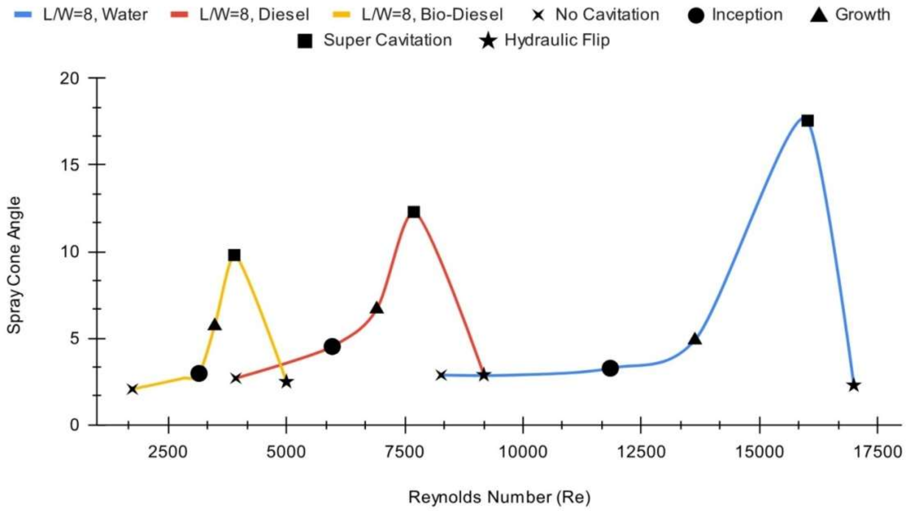

Fig 5.43 Reynolds number vs Spray cone angle (CN 5WDB)

The current experimental work used three fluids (water, diesel, and WCO-biodiesel) with two distinct nozzle dimensions (L/D = 4 and L/D = 8). Fig. 5.44 shows the collection of all experimental data and presents it in a single plot using Reynolds and cavitation numbers. In all instances, the cavitation number decreases with increasing Reynolds number. The rate of CN reduction changes after cavitation begins, and the CN curve becomes asymptotic when the hydraulic flip occurs. The curves shifted inward as the L/W ratio fell from 8 to 4. It demonstrates that as L/W decreases the onset of cavitation, super cavitation occurs at a lower Reynolds number. A lower Reynolds number indicates lower exit velocity and injection pressure. It is concluded that reducing the L/W ratio demands less pressure to produce super cavitation. The cavitation begins when the cavitation number falls below unity, regardless of geometrical parameters or fluid properties. Although vapor pressure affects the inception of cavitation and it starts at lower cavitation number. The fluid viscosity has a significant effect on the Reynolds number and cavitation number. As viscosity increased, curves moved inwards. The higher viscosity delayed the inception of cavitation, resulting in bubbles appearing at relatively lower cavitation numbers.

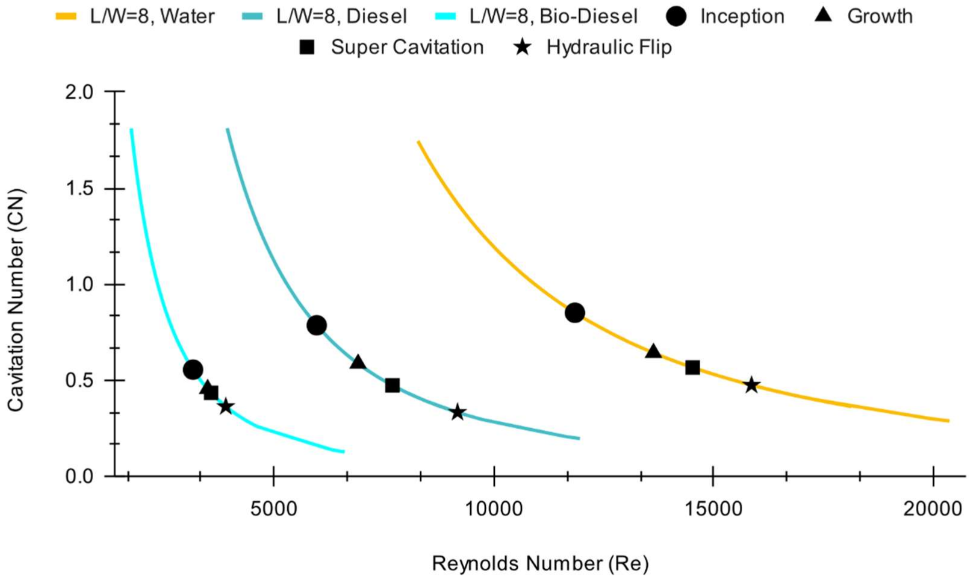

Fig 5.44 Reynolds number vs Cavitation number (CN 5WDB)

The different parameters can be computed at the inlet and outlet using the experiments stated above, however, it is difficult to acquire specifics of the parametric variation inside the nozzle. Computational fluid dynamics (CFD) can be very useful in determining the fluctuation in flow parameters under certain boundary conditions. The current experimental study can help identify CFD's initial and boundary conditions. A computational study was conducted for an acrylic nozzle utilizing diesel fuel. Based on the experimental results, three inlet pressures (2.3 bar, 3.4 bar, and 4.8 bar) were employed to capture the inception, growth, and super cavitation stages.

Fig. 5.45 illustrates a comparison of experimental and CFD data. The contour of the vapor fraction is compared to the image obtained during the experiment. The length of the vapor fraction inside the nozzle corresponds closely to the experimental image. The pressure contours indicate that negative values cause cavitation. The length of cavitation is directly proportional to the negative pressure zone inside the nozzle. The last outcome depicts the velocity contour. It signifies that the maximum velocity occurs near the centre of the nozzle.

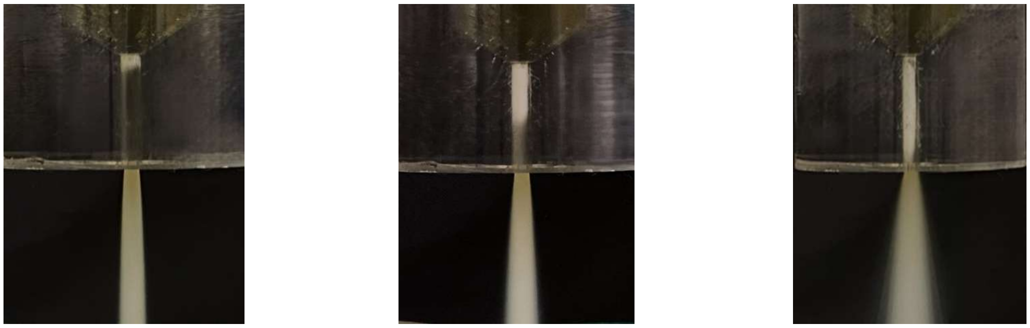

Cavitation stages and diesel spray

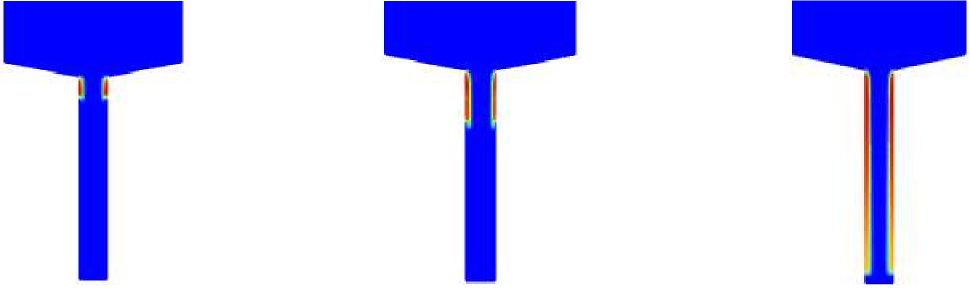

Vapor fraction contor

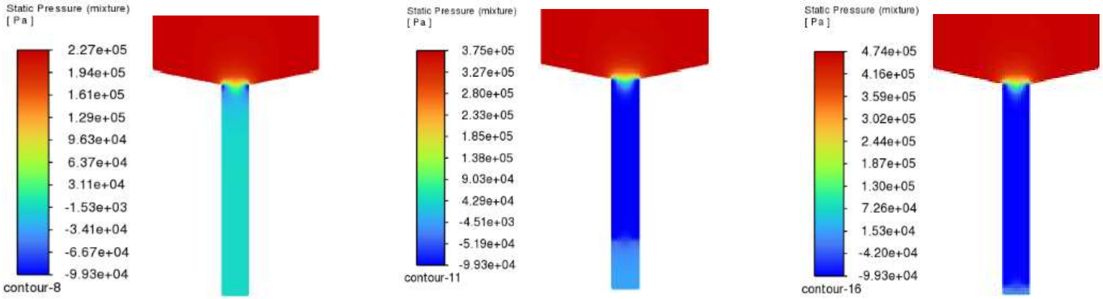

Pressure contour

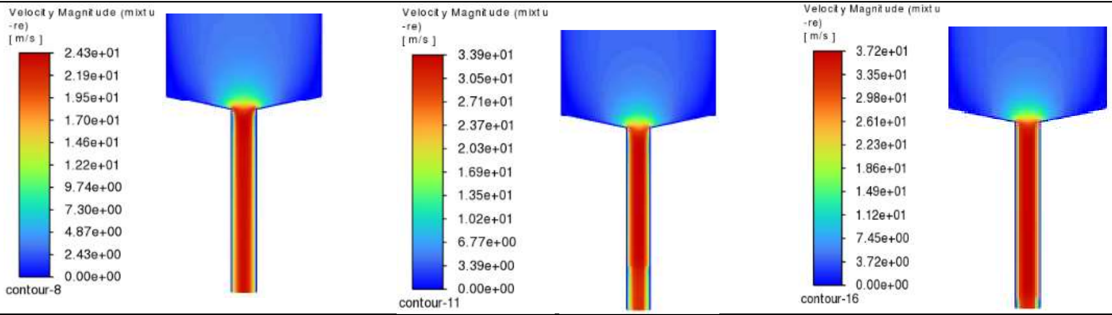

Velocity contour

Fig 5.45 Comparision of CFD results with experimental image for diesel fuel (CN 3D)

Fig. 5.46 depicts the distribution of pressure along the axis at various injection pressures. The pressure in the upstream region of the nozzle is almost constant. The pressure abruptly drops, reaching a negative value at the nozzle inlet. The negative pressure will return due to the atmospheric outlet situation. Higher injection pressure results in a deeper fall and increased cavitation. Fig. 5.47(a) and (b) depict velocity profiles at the nozzle's inlet and outlet, respectively. Because of cavitation, the vapor bubbles move faster than the liquid core displayed. Due to cavitation, the velocity of vapor bubbles is higher near the wall than that of the liquid core shown in Fig. 5.47(a). At the outlet, in the absence of vapor, a normal velocity profile is observed.

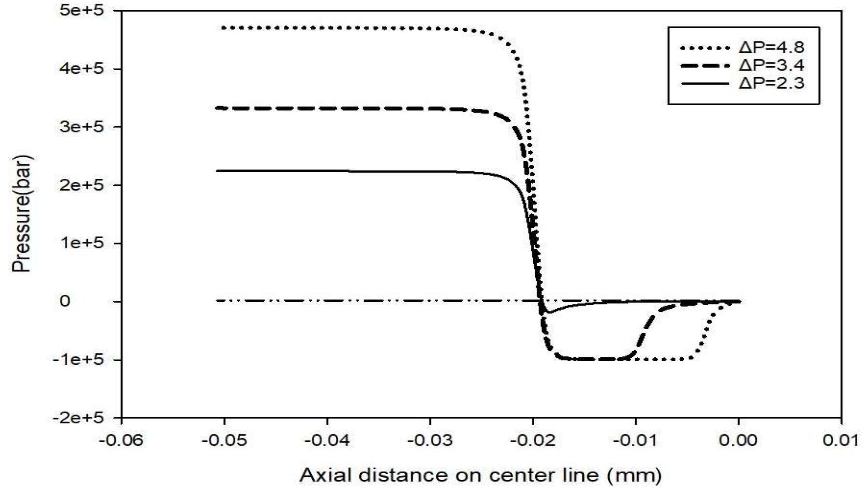

Fig 5.46 Pressure distribution along the axis

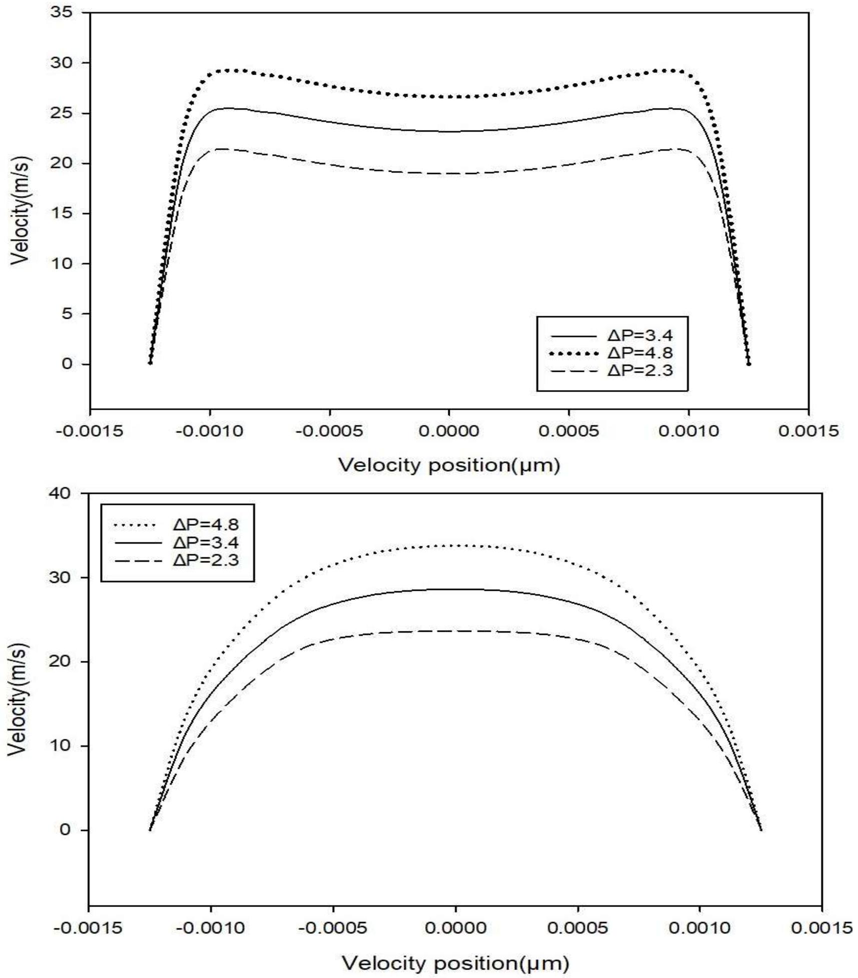

Fig. 5.47 Velocity profile at (a) Inlet of the nozzle (b) Outlet of the nozzle

5.4 EXPERIMENTAL RESULTS OF SPRAY CHARACTERISTICS

The study of fuel spray characteristics of diesel and bio-diesel has become increasingly important in recent years due to the need for more sustainable and environmentally friendly transportation technologies. However, the use of biodiesel fuels also presents technical challenges related to engine performance and durability. For an instant, biodiesel fuels have higher viscosity and lower energy density as compared to conventional diesel, which can result in lower engine efficiency and increases wear and tear on engine components. In order to optimize the performance and efficiency of diesel engines running on biodiesel, it is crucial to understand the fuel spray characteristics of both diesel and biodiesel fuels. The spray characteristics, such as spray penetration, cone angle and droplet size distribution, can significantly affect the combustion process, emissions and engine performance. Understanding the spray characteristics of diesel and biodiesel fuels can provide important insights into potential of biodiesel fuels to address current environmental and technical challenges related to diesel engine technology. Current section reported the results of spray characteristics using diesel, tallow biodiesel and WCO biodiesel. Fig. 5.48 shows the image processing steps which discussed in section 3.5.1, chapter 3.

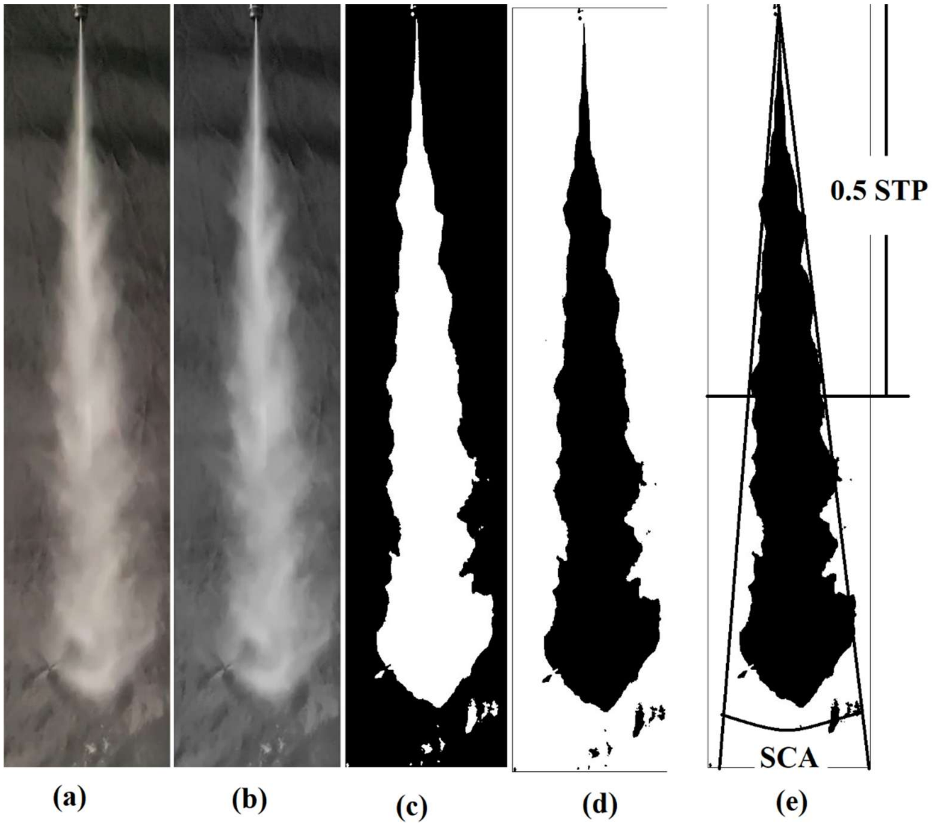

Fig 5.48 Image processing steps

The spray characteristics were investigated using a single-hole common rail fuel injector manufactured by Delphi. The solenoid-operated needle controls the start (SOI) and end of injection (EOI). The fuel was injected with three different injection pressures (150, 300, and 500 bar) and an injection time of 2 ms. It is necessary to take an intermediate still image of the spray during a single injection event. The fuel injection is filmed with a high-speed camera (1000 frames per second) and then slowed down with an image processing program (ADOBE Pro). The still image was recorded every 0.2 ms, and additional image processing was performed to determine spray tip penetration (STP) and spray cone angle. Fig. 5.48(a) shows the raw image captured by the camera, which is converted into a greyscale image as shown in Fig. 5.48(b). The greyscale image was then converted into a binary image to detect the spray boundary, as shown in Fig. 5.48(c). Finally, spray cone angle and spray tip penetration are measured by inverting the colour of the binary image, as shown in Fig. 4.48 (c) and Fig. 4.48(d).

5.4.1 Spray development

Fig. 5.49 depicts the spray development of diesel spray under different injection pressures. As injection pressure increases, the spray border becomes unstable, and ligament breakage is readily visible. Figure 5.50 depicts spray formation for diesel, tallow biodiesel, and WCO-biodiesel at a pressure of 500 bar. Due to its high viscosity, biodiesel produces narrow spray. The spray area and volume are larger in the case of diesel spray.

5.4.2 Spray tip penetration (STP)

The penetration length of the diesel fuel spray as a function of time after the start of injection is shown in Fig. 5.51. Initial fuel penetrates quickly; after the spray breakup starts, the rate of penetration decreases. Spray tip penetration increases with injection pressure. The computed spray tip penetration is compared to the empirical equation proposed by Arai [112].

Figure 5.52 (a), (b), and (c) compare the spray tip penetration of diesel, tallow biodiesel, and WCO-biodiesel at 150 bar, 300 bar, and 500 bar, respectively. At the start of injection, all fuels have similar penetration lengths, but as time progresses, it can be observed that the tallow biodiesel spray has a shorter penetration length compared to diesel fuel. Although the WCO-based biodiesel shows greater spray tip penetration as compared to diesel fuel, this is likely due to the differences in the physical properties of the fuel, such as viscosity and surface tension, which affect the spray behaviour.

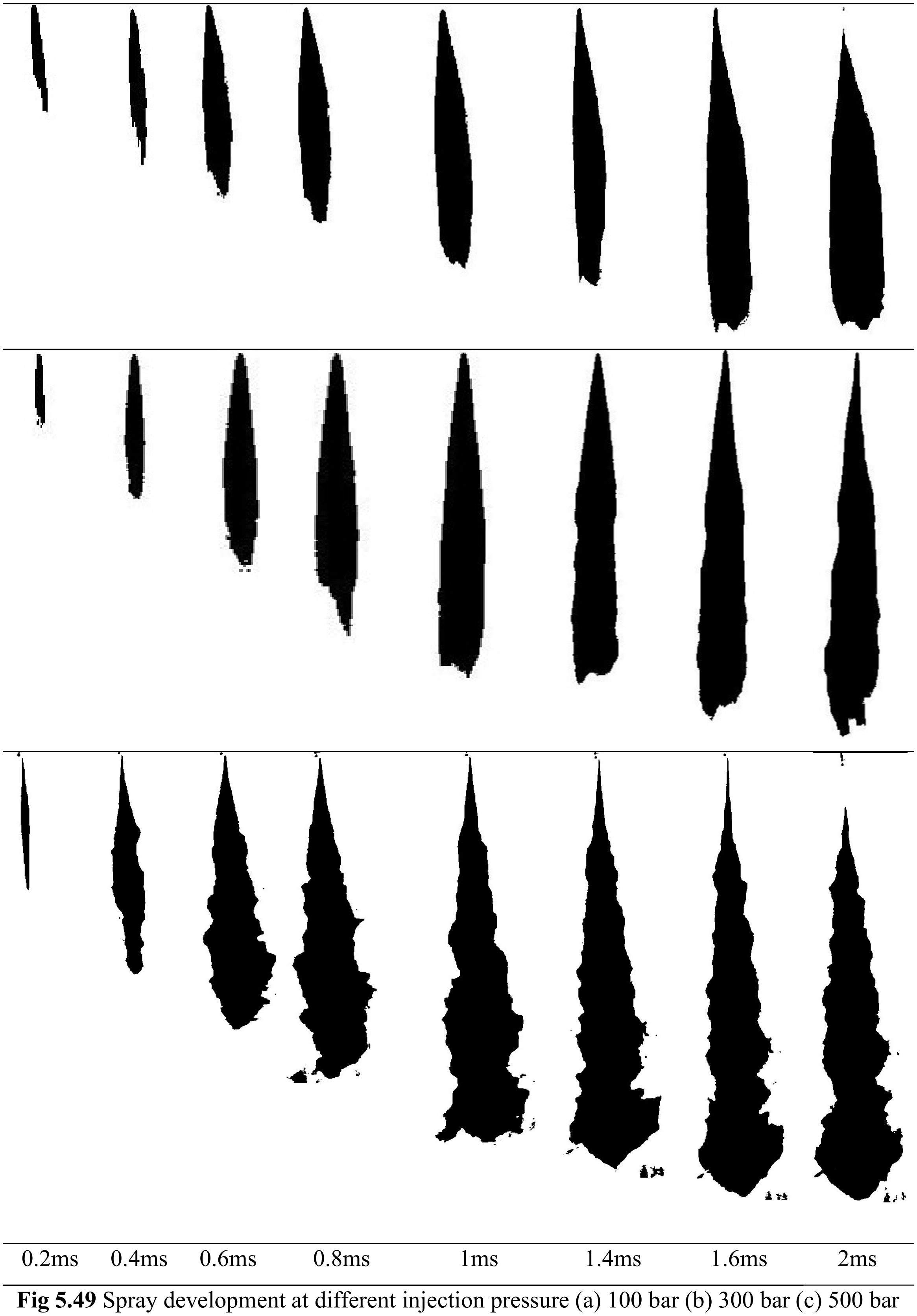

Fig 5.49 Spray development at different injection pressure (a) 100 bar (b) 300 bar (c) 500 bar

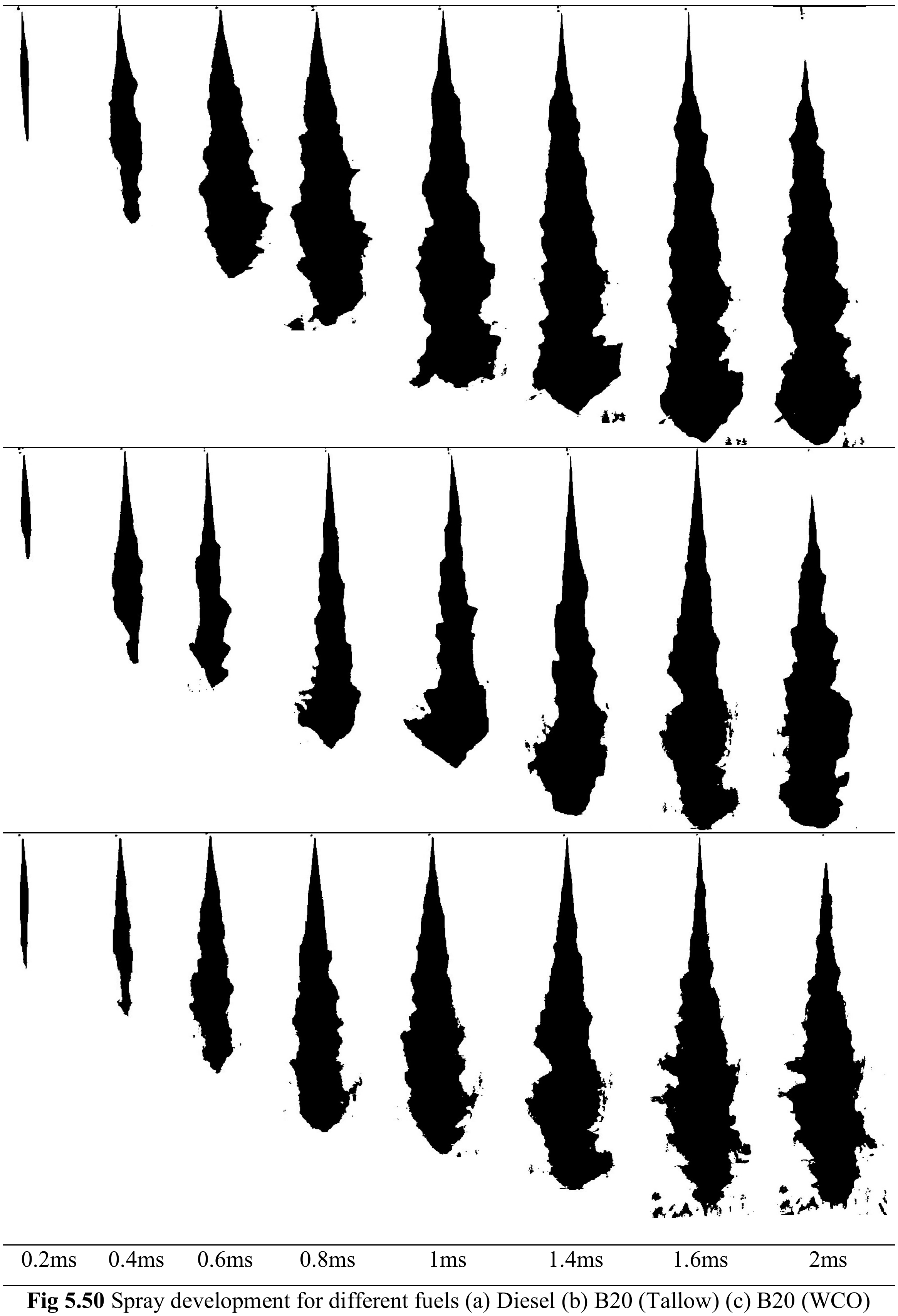

Fig 5.50 Spray development for different fuels (a) Diesel (b) B20 (Tallow) (c) B20 (WCO)

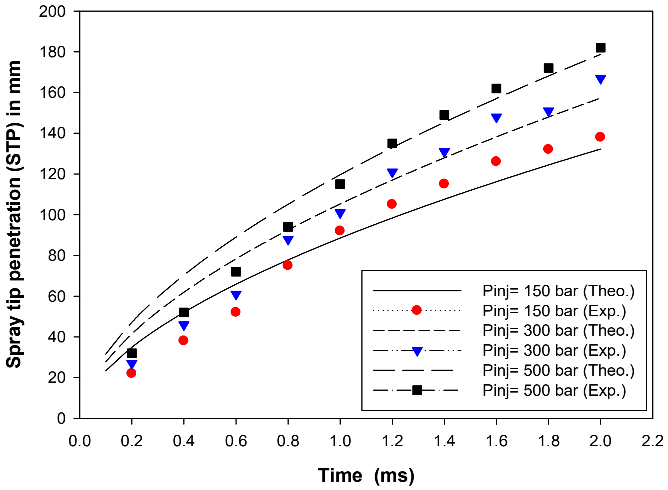

Fig 5.51 Spray tip penetration of diesel fuels at different injection pressure

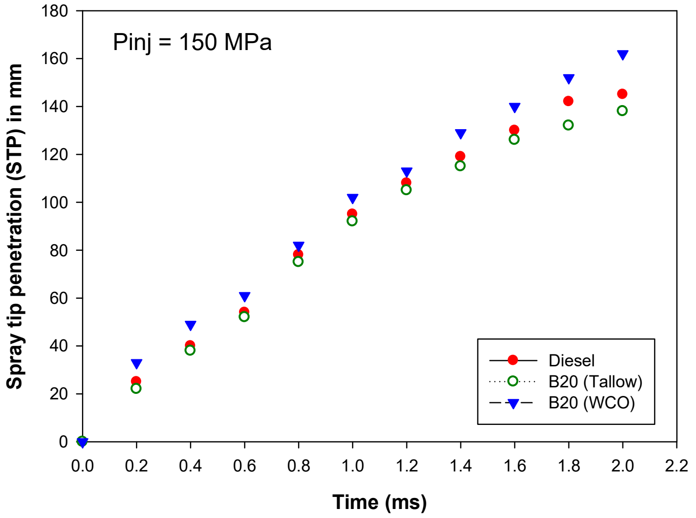

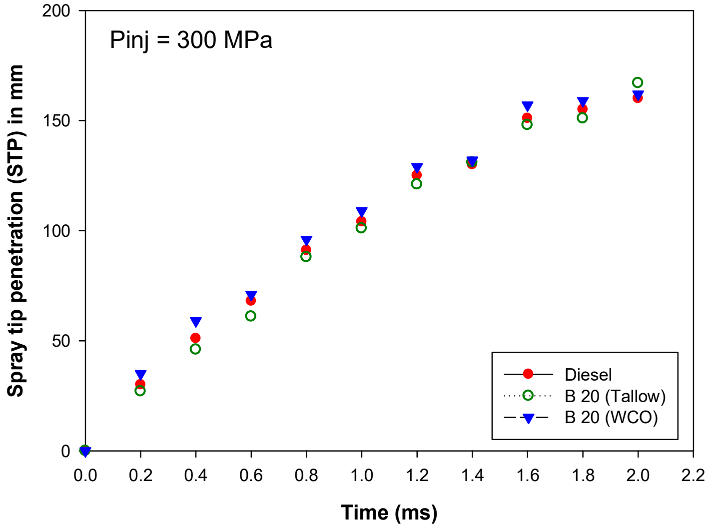

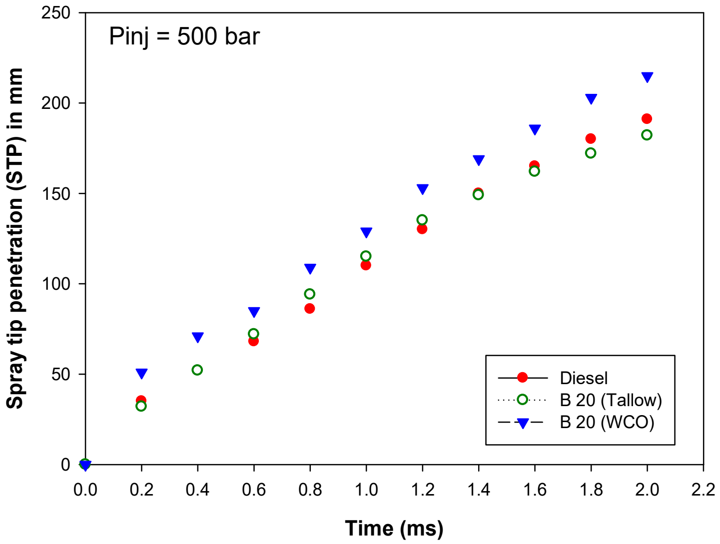

Fig 5.52 Spray tip penetration foe diesel, tallow & WCO (a) 150 bar (b) 300 bar (c) 500 bar

5.4.3 Spray cone angle (SCA)

The spray cone angle has been measure using still image of the spray at different time interval. It is observed that initially large fluctuation in the spray cone angle observed, although after breakup time (t= 1.2 ms) spray becomes more stable shown in Fig 5.53. The spray cone angle is measured using the image capture after 1.2 ms SOI at the injection pressure of 500 bar. The average values of are considered as a final spray cone angle. The spray cone angle of diesel, tallow biodiesel and WCO biodiesel are 17˚, 15.4˚ and 15.6˚ respectively. Biodiesel is projected a lower spray cone angle than diesel spray. Spray characteristics are essentially identical in tallow and WCO biodiesel.

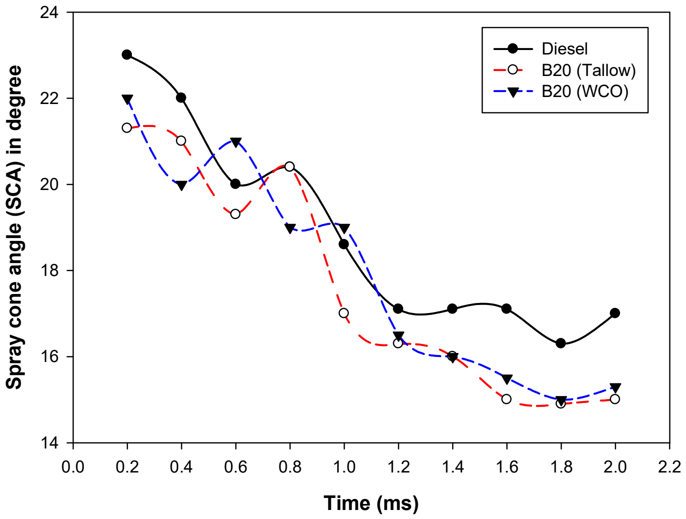

Fig 5.53 Spray cone angle at different time interval

5.5 OUTCOME OF THE CURRENT RESEARCH

In this research, a two-step coupling method has been developed to accurately predict the effect of cavitation flow on spray characteristics. This approach has been successfully implemented in experiments conducted to analyse spray behaviour. The spray simulations were carried out using two different methodologies: (1) the conventional method, where the mass flow rate and nozzle diameter were directly provided as inputs based on experimental conditions, and (2) the proposed two-step coupled method, where only the injection pressure was specified, allowing the model to inherently capture the influence of cavitation on spray formation. The results indicate (Fig 5.54) that the spray cone angle predicted by the two-step coupled method closely matches the experimental observations, whereas the conventional method fails to account for the impact of cavitation, leading to deviations from experimental findings. This discrepancy highlights the limitation of traditional approaches, which do not incorporate cavitation-induced flow effects on spray breakup and atomization. By contrast, the proposed method successfully bridges this gap by integrating the cavitation dynamics into spray modelling.

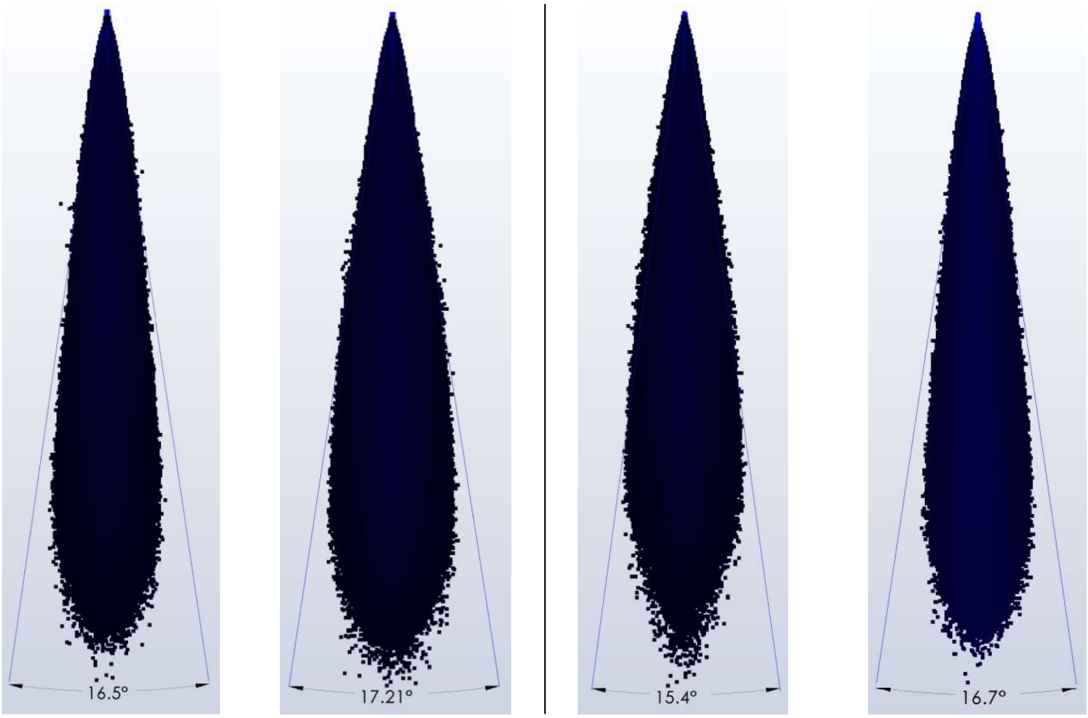

$\theta=16.5^{\circ}$	$\theta=17.2^{\circ}$	$\theta=15.4^{\circ}$	$\theta=16.7^{\circ}$
$\theta_{exp}=17$		$\theta_{exp}=16.6^{\circ}$	
(Convectional Method)	(Two-step coupled Method)	(Convectional Method)	(Two-step coupled Method)
Diesel		WCO-biodiesel	

Fig 5.54 Calculation of SCA using two-step coupled method

This research provides a significant advancement in fuel injector modelling, as the two-step coupled method enables a more accurate prediction of spray characteristics under cavitating conditions. The ability to capture the influence of cavitation on spray formation is crucial for optimizing fuel injection systems, especially for biodiesel applications where cavitation plays a vital role in enhancing atomization. The developed methodology can be effectively implemented in fuel injector design, improving combustion efficiency and performance by ensuring better air-fuel mixing and droplet distribution.

L/D ratio	Inception of Cavitation	Super cavitation
L/d=8.18 (L=19.32mm, d=2.36mm)	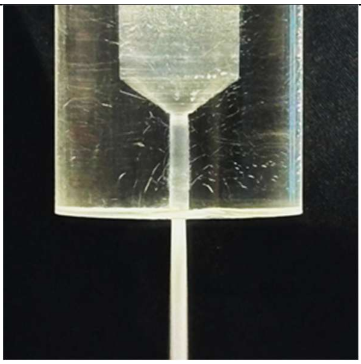	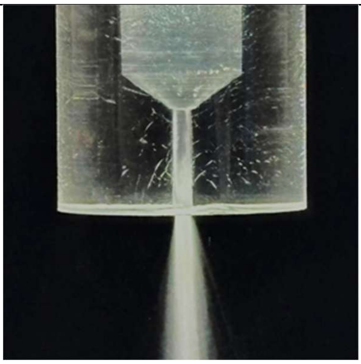
L/d=6.684 (L=16.71mm, d=2.36mm)	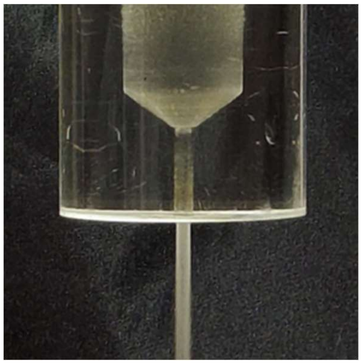	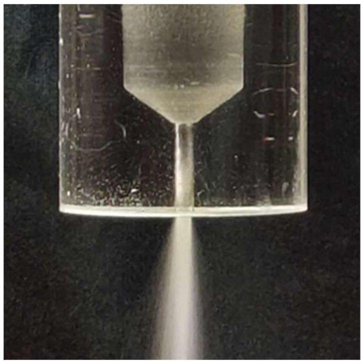
L/d=5.34 (L=12.6mm, d=2.36mm)	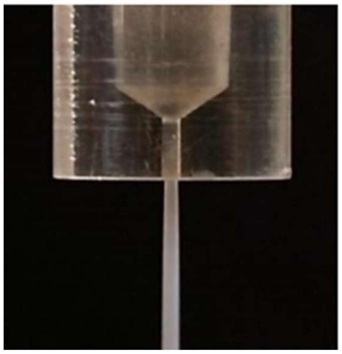	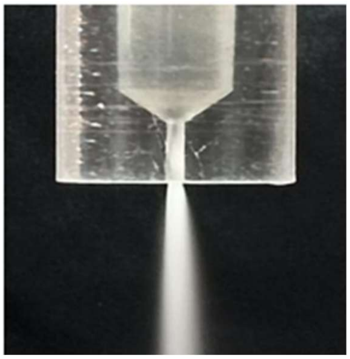

Fig 5.55 Cavitation inception and super cavitation at different L/d ratio

The cavitation phenomenon in fuel injector nozzles is influenced by both nozzle geometry (length and diameter) and operating conditions. To represent these factors in a non-dimensional form, the length-to-diameter (L/D) ratio and cavitation number (CN) are used as key parameters. In this study, experiments were conducted across different L/D ratios ranging from 4 to 8 as shown in Fig 5.55, leading to the development of a cavitation map that classifies different cavitation stages—namely inception, development, and super cavitation. Based on these experimental results, empirical models have been proposed to predict cavitation behaviour shown in Fig 5.56.

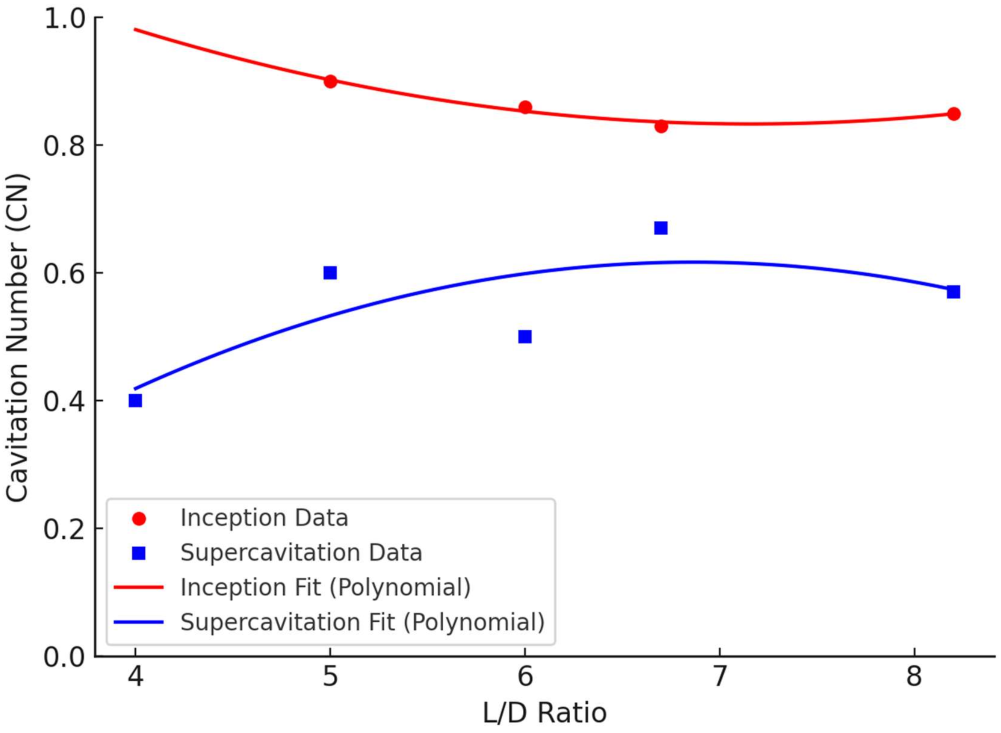

Fig 5.56 Cavitation number vs L/d ratio

The following empirical equations were developed using polynomial curve fitting to predict the cavitation inception and super cavitation conditions based on L/D ratio.

$$Cavitation\ Inception: CN_{inception} = 0.0148\left(\frac{L}{d}\right)^2 - 0.2118\left(\frac{L}{d}\right) + 1.5911$$

$$Super\ cavitation: CN_{super\ cav} = -0.0241\left(\frac{L}{d}\right)^2 + 0.3307\left(\frac{L}{d}\right) - 0.5186$$

One of the key findings of this research is the development of two empirical equations based on cavitation map, that characterize cavitation behavior in fuel injector nozzles. The first equation predicts the cavitation inception condition based on the nozzle's geometric (L/D ratio) and operating parameters, allowing the identification of whether the injector operates in a cavitating or non-cavitating regime. This is crucial for optimizing fuel injection systems to enhance atomization and combustion efficiency. Since this study focuses on biodiesel, the second empirical equation provides insights into achieving super cavitation, which has been shown to improve spray characteristics and overall engine performance. Super cavitation can mitigate the drawbacks associated with biodiesel, such as poor atomization and higher viscosity, by promoting finer droplet formation and better air-fuel mixing. These equations serve as valuable predictive tools for injector design and operational optimization, ensuring improved combustion characteristics and enhanced efficiency in biodiesel-fuelled engines.